

## Temperature limits to deep seafloor life in the Nankai Trough subduction zone

V. B. Heuer,<sup>1\*</sup> F. Inagaki,<sup>2,3\*</sup> Y. Morono,<sup>3\*</sup> Y. Kubo,<sup>4,a</sup> A. J. Spivack,<sup>5</sup> B. Viehweger,<sup>1</sup> T. Treude,<sup>6</sup> F. Beulig,<sup>7,b</sup> F. Schubotz,<sup>1</sup> S. Tonai,<sup>8</sup> S. A. Bowden,<sup>9</sup> M. Cramm,<sup>10</sup> S. Henkel,<sup>11</sup> T. Hirose,<sup>3</sup> K. Homola,<sup>5</sup> T. Hoshino,<sup>3</sup> A. Ijiri,<sup>3</sup> H. Imachi,<sup>12</sup> N. Kamiya,<sup>13,c</sup> M. Kaneko,<sup>14</sup> L. Lagostina,<sup>15,d</sup> H. Manners,<sup>16</sup> H.-L. McClelland,<sup>17,e</sup> K. Metcalfe,<sup>18</sup> N. Okutsu,<sup>19,f</sup> D. Pan,<sup>20,g</sup> M. J. Raudsepp,<sup>21,h</sup> J. Sauvage,<sup>5,i</sup> M.-Y. Tsang,<sup>22</sup> D. T. Wang,<sup>23,j</sup> E. Whitaker,<sup>24</sup> Y. Yamamoto,<sup>25,k</sup> K. Yang,<sup>26,l</sup> L. Maeda,<sup>4</sup> R. R. Adhikari,<sup>1</sup> C. Glombitza,<sup>27</sup> Y. Hamada,<sup>3</sup> J. Kallmeyer,<sup>28</sup> J. Wendt,<sup>1</sup> L. Wörmer,<sup>1</sup> Y. Yamada,<sup>2</sup> M. Kinoshita,<sup>29</sup> K.-U. Hinrichs<sup>1§</sup>

\*V.B.H, F.I., and Y.M. contributed equally to this work.

<sup>§</sup>Corresponding author: E-mail: khinrichs@uni-bremen.de (K.-U.H.)

One sentence summary: In deep seafloor sediments above 45°C microbial cells are rare, endospores prevail, and life still persists at 120°C.

<sup>1</sup>Center for Marine Environmental Sciences (MARUM), University of Bremen, Bremen, Germany

<sup>2</sup>Research and Development Center for Ocean Drilling Science (ODS), Japan Agency for Marine-Earth Science and Technology, Yokohama, Japan

<sup>3</sup>Kochi Institute for Core Sample Research (KCC), Japan Agency for Marine-Earth Science and Technology, Kochi, Japan

<sup>4</sup>Center for Deep Earth Exploration (CDEX), Japan Agency for Marine-Earth Science and Technology, Yokohama, Japan

<sup>5</sup>Graduate School of Oceanography, University of Rhode Island, Narragansett, USA

<sup>6</sup>Department of Earth, Planetary, and Space Sciences, Department of Atmospheric and Oceanic Sciences, University of California, Los Angeles (UCLA), Los Angeles, USA

<sup>7</sup>Center for Geomicrobiology, Department of Bioscience, Aarhus University, Aarhus, Denmark

<sup>8</sup>Faculty of Science and Technology, Kochi University, Kochi, Japan

<sup>9</sup>Department of Geology and Petroleum Geology, School of Geosciences, University of Aberdeen, Aberdeen, United Kingdom

<sup>10</sup>Department of Biological Sciences, University of Calgary, Calgary, Canada

<sup>11</sup>Alfred Wegener Institute, Helmholtz Centre for Polar and Marine Research, Bremerhaven, Germany

<sup>12</sup>Institute for Extra-cutting-edge Science and Technology Avantgarde Research, Japan Agency for Marine-Earth Science and Technology, Yokosuka, Japan

<sup>13</sup>Graduate School of Integrated Basic Sciences, Nihon University, Tokyo, Japan

<sup>14</sup>Geomicrobiology Research Group, National Institute of Advanced Industrial Science and Technology (AIST), Tsukuba, Japan

<sup>15</sup>Department of Environmental Systems Science, ETH Zürich, Zürich, Switzerland

<sup>16</sup>School of Geography, Earth and Environmental Sciences, Faculty of Science and Engineering, Plymouth University, Plymouth, United Kingdom

<sup>17</sup>Department of Earth and Planetary Sciences, Washington University in St. Louis, St. Louis, USA

<sup>18</sup>Division of Geological and Planetary Sciences, California Institute of Technology, Pasadena, USA

- <sup>19</sup>Atmosphere and Ocean Research Institute, University of Tokyo, Tokyo, Japan
- <sup>20</sup>Department of Subsurface Geobiological Analysis and Research, Japan Agency for Marine-Earth Science and Technology, Yokosuka, Japan
- <sup>21</sup>School of Earth Sciences, University of Queensland, St. Lucia, Australia
- <sup>22</sup>Department of Earth Sciences, University of Toronto, Toronto, Canada
- <sup>23</sup>Department of Earth, Atmospheric and Planetary Sciences, Massachusetts Institute of Technology, Cambridge, USA
- <sup>24</sup>Department of Oceanography, Texas A&M University, College Station, USA
- <sup>25</sup>Department of Mathematical Science and Advanced, Technology (MAT), Japan Agency for Marine-Earth Science and Technology, Yokosuka, Japan
- <sup>26</sup>Department of Earth System Sciences, Yonsei University, Seoul, Republic of Korea
- <sup>27</sup>Institute of Biogeochemistry and Pollutant Dynamics, ETH Zürich, Zürich, Switzerland
- <sup>28</sup>Helmholtz Centre Potsdam, GFZ German Research Centre For Geosciences, Potsdam, Germany
- <sup>29</sup>Earthquake Research Institute, University of Tokyo, Tokyo, Japan

Present address:

- <sup>a</sup>Kochi Institute for Core Sample Research (KCC), Japan Agency for Marine-Earth Science and Technology, Kochi, Japan
- <sup>b</sup>Department of Ecological Microbiology, University of Bayreuth, Bayreuth, Germany
- <sup>c</sup>Graduate School of Engineering, Kyoto University, Kyoto, Japan
- <sup>d</sup>Robert Koch-Institut, Berlin, Germany
- <sup>e</sup>School of Earth Sciences, University of Melbourne, Melbourne, Australia
- <sup>f</sup>Institute for Marine-Earth Exploration & Engineering, Japan Agency for Marine-Earth Science and Technology, Yokohama, Japan
- <sup>g</sup>Department of Ecology & Environmental Studies, The Water School, Florida Gulf Coast University, Fort Myers, USA
- <sup>h</sup>Department of Earth and Atmospheric Sciences, The University of Alberta, Edmonton, Canada
- <sup>i</sup>Department of Marine Sciences, University of Gothenburg, Gothenburg, Sweden
- <sup>j</sup>ExxonMobil, 22777 Springwoods Village Parkway, Spring, Texas 77389 USA
- <sup>k</sup>Graduate School of Geoscience, Kobe University, Kobe, Japan
- <sup>l</sup>Department of Oceanography, Pusan National University, Busan, Republic of Korea

1 **Abstract:** *Microorganisms in marine subsurface sediments substantially contribute to global biomass.*  
2 *Sediments warmer than 40°C account for ~half the volume of marine sediment, but the processes*  
3 *mediated by microbial populations in these hard-to-access environments are poorly understood. Here*  
4 *we demonstrate the presence and activity of microbial life in up to 1.2 km deep and up to 120°C hot*  
5 *sediments in the Nankai Trough subduction zone. Above 45°C, concentrations of vegetative cells drop*  
6 *two orders of magnitude, while endospores become more than 6,000 times more abundant than*  
7 *vegetative cells. Methane is biologically produced and oxidized until sediments reach 80-85°C. In*  
8 *100°C to 120°C hot sediments, isotopic evidence and elevated cell concentrations demonstrate the*  
9 *activity of acetate-degrading hyperthermophiles. Strikingly, above 45°C populated zones alternate*  
10 *with zones up to 192 m thick where microbes were undetectable.*

11 Scientific ocean drilling has demonstrated the ubiquity of microbial life in deep subseafloor  
12 environments down to 2.5 km below seafloor (1-3). As sediment temperature increases with burial  
13 depth, more than 50% of the global marine sediment volume is situated above 40°C (4). So far, the  
14 vast majority of subseafloor-life studies has targeted environments with in-situ temperatures <30°C,  
15 and consequently the habitability of hotter sediments is largely unexplored. Microbes with growth  
16 temperatures up to 122°C have been isolated at hydrothermal vents (5), where the metabolism of  
17 these hyperthermophiles is fueled by high fluxes of oxidants and reductants (6). However, in deeply  
18 buried sediments, the potential metabolic energy is limited and with increasing depth and  
19 temperature the slow-growing microbial communities struggle to meet the cellular maintenance  
20 energy requirement (3, 7, 8). Even in organic-matter rich petroleum reservoirs, microbial activity  
21 appears to cease at temperatures of ~80°C (9, 10).

22 Aiming to fill the vast knowledge gaps regarding the response of microbial life to increasing  
23 temperature, we investigated up to 1.2 km deep and up to 120°C hot sediments in the Nankai Trough  
24 off Cape Muroto, Japan (fig. S1). In this area, an up to 16 million year (My) old, ~600 m thick  
25 succession of hemipelagic mudstones and tuffs has been rapidly buried by an equally thick layer of  
26 trench deposits over the past ~0.4 My (11, 12; fig. S2). Sediments concurrently heated by  
27 approximately 50°C, and the onset of subduction formed a décollement separating the accreting and  
28 underthrust domains (11, 12). First indications for the presence of microbial life in ~800 m deep,  
29 ~80-90°C warm sediments at a nearby drill site date back two decades (12, 13). However, insufficient  
30 sensitivity in cell detection at that time compromised the habitability assessment of this environment  
31 (13). We designed Expedition 370 of the International Ocean Discovery Program (IODP) to achieve  
32 maximal sensitivity in life detection together with accurate determination of in-situ temperatures,  
33 and established Site C0023 (32°22.0018'N, 134°57.9844'E, 4776 m water depth; fig. S1) in the vicinity  
34 of the previous drill site (14). Rigorous precautions during sampling and improvements in cell  
35 enumeration techniques (11) increased the sensitivity in cell detection by five orders of magnitude  
36 compared to the previous study (13). For the quantification of cells that can be stained by a  
37 fluorescent dye (hereafter termed vegetative cells; ref. 11), the procedural blank was  $4.2 \pm 4.0$  cells  
38  $\text{cm}^{-3}$  of sediment (N = 20), thereby yielding a minimum quantification limit (MQL) of 16 cells  $\text{cm}^{-3}$   
39 (11). Temperature measurements in the borehole constrained a steady-state temperature profile  
40 with a gradient of  $110^\circ\text{C km}^{-1}$  and a temperature of  $120 \pm 3^\circ\text{C}$  in the deepest core retrieved from the  
41 basement at 1177 m below seafloor (mbsf) (11, figs. S3-4). The combination of authigenic minerals  
42 and thermally altered biomarkers reveals a history of episodic, short-term ingression of ~140-220°C  
43 hot hydrothermal fluids along permeable strata in the underthrust domain (15, fig. S2).

44 At Site C0023, the depth profile of cell concentrations deviates notably from the global trend of  
45 gradually decreasing cell concentrations observed in similarly deep but substantially colder (<30°C)  
46 sediments (1, 2). At ~300-400 mbsf, concentrations of vegetative cells drop abruptly by two orders of

47 magnitude and approach the MQL as temperature rises from 40°C to 50°C (Fig. 1A). Concurrently,  
48 concentrations of endospores, i.e., dormant, resistant structures affiliated with the bacterial phylum  
49 Firmicutes (fig. S5), which are widely found in marine sediments and soils (16, 17), increase to  
50  $2 \times 10^5 \text{ cm}^{-3}$  (Fig. 1B). Nevertheless, a small microbial population persists at >50°C in the form of both  
51 vegetative cells and endospores (Fig. 1). Down to the 120°C hot basement, sediments harboring  
52 microbial communities with up to 400 vegetative cells  $\text{cm}^{-3}$  are interspersed within intervals of up to  
53 192 m thickness, in which no cells were detected (Fig. 1A; fig. S6). We rule out the possibility that the  
54 detection of cells resulted from contamination because cell concentration is neither related to the  
55 abundance of fractures in sediment cores nor to the concentration of the perfluorocarbon-based  
56 contamination tracer supplied during drilling operation (11, fig. S7); such relationships would be  
57 expected if contaminant cells were introduced via drilling fluids. Consistent with the extremely low  
58 concentrations of vegetative cells and the difficulty of extracting DNA from endospores (18), DNA  
59 yields were insufficient for producing reliable DNA-based community data for samples buried more  
60 deeply than 320 mbsf (14). In samples shallower than 320 mbsf, the community resembled those  
61 found in shallow subsurface sediments (14).

62 In contrast to the scattered distribution of vegetative cells in sediments >50°C, endospores show a  
63 clear zonation (Fig. 1B), as quantified by measurement of the diagnostic biomarker dipicolinic acid  
64 (DPA) (11, 19). We rule out that substantial levels of DPA could have accumulated after the decay of  
65 endospores, given the propensity of 2-carboxylated pyridines to decarboxylate upon moderate short-  
66 term heating (20). Endospore concentrations rise prominently in a ~200-m interval of 75-90°C hot  
67 sediments, with a maximum of  $1.2 \times 10^6$  endospores  $\text{cm}^{-3}$  at 85°C. The average endospore-to-  
68 vegetative cell ratio exceeds 6,000 in sediments below 350 mbsf (11; table S1) and is thus 2-3 orders  
69 of magnitude higher than in cold subseafloor sediments (19). Plausible scenarios for the  
70 accumulation of endospores in sediments that are nearly barren of vegetative cells relate to the  
71 thermal history of the site since the onset of trench conditions ~0.4 My ago (11, 12) and involve the  
72 transitory growth of a thermophilic population of endospore formers (cf. ref. 17) after temperature  
73 rose to ~50°C and its subsequent sporulation (11, fig. S8). Interestingly, in two expanded horizons, at  
74 570-633 mbsf and 829-1021 mbsf, neither vegetative cells nor endospores were detected (Fig. 1, fig.  
75 S6).

76 Pore-water profiles of microbial substrates and products provide evidence for microbial activity  
77 down to the ~16 My old oceanic crust (Fig. 2). High concentrations of methane with a mean carbon  
78 isotopic composition ( $\delta^{13}\text{C}\text{-CH}_4$ ) of  $-61.3 \pm 3.0$  per mil (‰) (Fig. 2A-B) indicate biogenic  
79 methanogenesis at least down to the 80-85°C hot sulfate methane transition zone (SMTZ) at ~730  
80 mbsf. The positive excursion in  $\delta^{13}\text{C}\text{-CH}_4$  in the 80 to 85°C hot SMTZ (Fig. 2B) points to a biogenic  
81 methane sink and is consistent with previous observations from cultivation-based approaches that  
82 demonstrated the activity of thermophilic anaerobic methane-oxidizing communities at these  
83 temperatures (21-22). Below the SMTZ, methane is only present in micromolar concentrations, with  
84 rising  $\delta^{13}\text{C}\text{-CH}_4$  values and decreasing methane/ethane ratios indicating a relative increase of  
85 thermogenic hydrocarbons (Fig. 2B). Remarkably, a reversal of this trend at >1000 mbsf hints at a  
86 biogenic methane source above 100°C.

87 Diffusive profiles of pore-water constituents do not allow the distinction between current and recent  
88 in-situ biogeochemical processes, while radiotracer experiments specifically target on-going  
89 microbial activity, albeit with some unavoidable deviation from in-situ conditions. At Site C0023,  
90 radiotracer experiments reveal present-day methanogenic activity in 65% of the investigated samples  
91 (Fig. 2D). Potential rates of methanogenesis via  $\text{CO}_2$  reduction in sediments below 300 mbsf are  
92 generally below  $4 \text{ pmol cm}^{-3} \text{ d}^{-1}$  and thus within the range of previous observations made in the deep

93 subseafloor (23). Their depth distribution is consistent with cellular concentrations (Fig. 1) and  
94 activities deduced from the pore-water profiles of methane (Fig. 2A-B). Rates are highest in the  
95 methanic zone, decrease distinctly to  $<0.6 \text{ pmol cm}^{-3} \text{ d}^{-1}$  below the SMTZ, and drop to undetectable  
96 levels in 63% of the samples taken from the deep expanded horizon with no detectable cells and  
97 endospores (Fig. 2D). Strikingly, potential methanogenesis rates rise again to values observed in the  
98 methanic zone in the three deepest samples (Fig. 2D), thus confirming the existence of active  
99 methanogenic communities in 110-120°C hot sediments and pillow basalts above basement.

100 Acetate has been suggested to fuel microbial life in deeply buried, geothermally heated sediments  
101 (24). Throughout the sediment column of Site C0023, reactions degrading acetate via sulfate  
102 reduction and methanogenesis are exergonic, with Gibbs free energy yields becoming increasingly  
103 negative with depth (fig. S9; ref. 11). The concentrations of acetate and its carbon isotopic  
104 compositions ( $\delta^{13}\text{C}$ -acetate) (Fig. 2C) indicate distinct changes in acetate utilization with temperature  
105 and depth. In the up to 60°C hot upper 600 mbsf, low and invariable concentrations of acetate  
106 around  $26 \pm 22 \text{ }\mu\text{M}$  (N=19) imply its balanced microbial production and consumption, while the  
107 corresponding fluctuation of  $\delta^{13}\text{C}$ -acetate around  $-25.5 \pm 3.4\text{‰}$  is consistent with various metabolic  
108 pathways influencing its pool (25). In sharp contrast, acetate utilization is minimal at 60°C to 100°C.  
109 At 60-75°C, acetate concentrations rise steeply with the simultaneous decline of methane  
110 concentrations and accumulation of endospores. A local minimum in acetate concentration at the  
111 SMTZ (Fig. 2C) is consistent with some microbial utilization at this geochemical interface. Below the  
112 SMTZ, acetate concentrations level at  $9.2 \pm 2.4 \text{ mM}$  with an invariable  $\delta^{13}\text{C}$ -acetate  
113 around  $-18.8 \pm 0.5\text{‰}$ . The combination of high concentration and low isotopic variability implies an  
114 acetate pool without significant turnover within the endospore-dominated zone as well as in the  
115 underlying 200 m thick zone, where neither cells nor endospores were detected.

116 At >1030 mbsf, however, acetate concentrations decline and  $\delta^{13}\text{C}$ -acetate monotonically increases  
117 with depth, reaching a maximum of  $-7.9\text{‰}$  in the deepest pore-water sample recovered from  
118 1101 mbsf. This trend is consistent with active hyperthermophiles degrading preferentially  $^{13}\text{C}$ -  
119 depleted acetate, leaving the residual acetate isotopically enriched. Without continued consumption,  
120 diffusion would homogenize  $\delta^{13}\text{C}$ -acetate variations, as observed in the overlying sediments. The  
121 drawdown of the acetate pool requires isotopic fractionation factors of  $-7.7$  to  $-15.4\text{‰}$  (11, fig. S10),  
122 which are consistent with those observed in lab cultures (26). The size of the sink would have to be  
123 on the order of  $5 \times 10^{-12} \text{ mol cm}^{-3} \text{ year}^{-1}$  (11). Given cellular concentrations of 10 to  $100 \text{ cm}^{-3}$  in  
124 sediments corresponding to this acetate sink, the required cellular metabolic rates are 2-3 orders of  
125 magnitude lower than observed in lab cultures of the hyperthermophilic archaea *Pyrococcus furiosus*  
126 (27) and *Archaeoglobus fulgidus* (28). Thus, acetate profiles are consistent with the existence of a  
127 small acetate-utilizing microbial community at >100°C. Acetate oxidation and syntrophic  
128 consumption of the resulting  $\text{CO}_2$  and electrons by methanogens are a known acetate sink in deep  
129 sediments (29) and at elevated temperatures (30). This process is exergonic under in-situ conditions  
130 (fig. S9) and could account for the elevated methanogenesis rates (Fig. 2D) and the isotopic signature  
131 of methane (Fig. 2B) in the deepest portion of the borehole.

132 Our findings reveal the impact of increasing temperature with depth on microbial life. This is  
133 exemplified in the massive collapse of the population of vegetative cells in <0.4 My old sediments at  
134 300-400 mbsf. In this interval, temperatures of 40-50°C are within the upper growth range of  
135 mesophiles. The coincident accumulation of endospores as a result of a putative sporulation of  
136 mesophilic endospore-forming Firmicutes (Fig. 1) supports the conclusion that the abundance and  
137 activity of microbial populations is primarily controlled by temperature-dependent physiological  
138 factors down to 600 mbsf. In the deeper portion of Site C0023 geological processes exert additional

139 control. A sharp decline in biogenic methanogenesis and acetate utilization at 70°C to 75°C coincides  
140 with the upper growth range of thermophiles, but notably, this depth interval concurrently spans the  
141 lithological boundary between Upper and Lower Shikoku Basin (cf. Fig. 1). At this boundary, tuffs  
142 (indurated volcanic ash) cease to be present. Tuff alteration forms smectite, and microbial reduction  
143 of Fe(III) in smectite serves as an energy yielding process and has in fact been found to promote  
144 smectite-to-illite conversion at 500-600 mbsf at Site C0023 (31). Thus, a modulation of the down-hole  
145 profile of microbial activity by microbe-mineral interactions is conceivable. Peak endospore  
146 concentrations at 85°C coincide with both the SMTZ and the plate boundary décollement. While  
147 frictional heating to temperatures of potentially up to ~1000°C (32) during plate motion likely causes  
148 additional challenges for microorganisms in this zone, endospores and high acetate concentrations  
149 provide a seed bank and energy, respectively, for an ecosystem recovery from episodic  
150 perturbations.

151 In the upper 200 m of the underthrust domain, at ~90-100°C, an expanded zone without detectable  
152 cells and with no geochemical signs of microbial activity traverses the sparsely populated sediments  
153 (Figs. 1, 2). In this zone, under-compacted and mechanically weak sediments are overpressurized and  
154 affected by ~145-220°C hot fluids for short durations (15, 33). The short heating events may have  
155 locally sterilized sediment (15), but microbial cells, acetate consumption and methanogenic activity  
156 prevail again in >100°C sediments, where mechanical strength and salinity increase towards the  
157 sediment/basement interface (Figs. 1, 2, fig. S2). Hydraulic communication between basalts and  
158 overlying sediment is evidenced by shared styles of epigenetic mineralization in the form of calcite  
159 veins and ferruginous metal oxides. Mass transfer between basal sediment and a basalt-hosted  
160 aquifer, would increase the habitability of the basal sediment by reducing formation fluid pressure,  
161 and replenishing otherwise depleted substrates such as reduced iron and sulfate (34).

162 Our study reveals the dependence of microbial abundance and activity to critical temperatures  
163 around 40-50°C and 70°C; it moreover shows that life in the deep seafloor is not constrained by  
164 an upper temperature limit below 120°C. Our findings highlight the interplay of geological processes,  
165 temperature and microbial life in the deep, hot sediments of the Nankai Trough, and suggest a  
166 critical influence of subduction-related geological processes on habitability.

**Acknowledgments.** This research used samples and data provided by the International Ocean Discovery Program (IODP). The authors are grateful to IODP and the Ministry of Education, Culture, Sports, Science and Technology of Japan (MEXT) for providing an opportunity to explore the deep biosphere during Expedition 370. The expedition comprised simultaneous offshore and onshore work, conducted on the drilling vessel *Chikyu* and in the Kochi Core Center (KCC), respectively. We thank all operational and technical staff members who have put our plans into action onboard *Chikyu* and at KCC. In particular, we would like to thank N. Eguchi, M. Kyo, and I. Sawada for their knowledgeable support during project design, and T. Saruhashi and K. Aoike for care- and successful drilling operations. This is a contribution to the Deep Carbon Observatory (DCO).

**Funding.** This work was supported in part by the Japan Society for the Promotion of Science (JSPS) Strategic Fund for Strengthening Leading-Edge Research and Development (to JAMSTEC and F.I.), the JSPS Funding Program for Next Generation World-Leading Researchers (GR102 to F.I.), the Deutsche Forschungsgemeinschaft through projects 387745511 (to V.B.H.), 408178672 (to F.S.), grant 408249062 (to J.K.), grant 279667358 and Hi 616-14-1 (to K.-U.H.) and through the Cluster of Excellence “The Ocean Floor – Earth’s Uncharted Interface” (project 390741603), the IODP U.S. Science Support Program (National Science Foundation prime award OCE-1450528 to T.T.), and the Natural Environment Research Council awards NE/P015182/1 and NE/R003408/1 (to S.A.B. and H.M., respectively). Additional support enabling this project was provided by the Deep Carbon Observatory.

**Data availability.** All shipboard and shore-based data presented in this manuscript are archived and publicly available online in the IODP Expedition 370 Proceedings (14), through the J-CORES database (<http://sio7.jamstec.go.jp/j-cores.data/370/C0023A/>) and the PANGAEA database (<http://doi.pangaea.de/10.1594/xxxx>).

**Competing interests.** None.

**Obligatory IODP related key words:** International Ocean Discovery Program, *DV Chikyu*, Expedition 370, Temperature Limit of the Deep Biosphere off Muroto, T-Limit, Site C0023.

## References and Notes

1. J. Kallmeyer, R. Pockalny, R. R. Adhikari, D. C. Smith, S. D'Hondt, Global distribution of microbial abundance and biomass in subseafloor sediment. *Proc. Natl. Acad. Sci. U. S. A.* **109**, 16213-16216 (2012).
2. R. J. Parkes *et al.*, A review of prokaryotic populations and processes in sub-seafloor sediments, including biosphere:geosphere interactions. *Mar. Geol.* **352**, 409-425 (2014).
3. F. Inagaki *et al.*, Exploring deep microbial life in coal-bearing sediment down to ~2.5 km below the ocean floor. *Science* **349**, 420-424 (2015).
4. D. E. LaRowe, E. Burwicz, S. Arndt, A. W. Dale, J. P. Amend, Temperature and volume of global marine sediments. *Geology* **45**, 275-278 (2017).
5. K. Takai *et al.*, Cell proliferation at 122 degrees C and isotopically heavy CH<sub>4</sub> production by a hyperthermophilic methanogen under high-pressure cultivation. *Proc. Natl. Acad. Sci. U. S. A.* **105**, 10949-10954 (2008).
6. J. P. Amend, E. L. Shock, Energetics of overall metabolic reactions of thermophilic and hyperthermophilic Archaea and Bacteria. *FEMS Microbiol. Rev.* **25**, 175-243 (2001).
7. M. A. Lever *et al.*, Life under extreme energy limitation: a synthesis of laboratory- and field-based investigations. *FEMS Microbiol. Rev.* **39**, 688-728 (2015).
8. M. H. Møller *et al.*, D:L-amino acid modeling reveals fast microbial turnover of days to months in the subsurface hydrothermal sediment of Guaymas Basin. *Front. Microbiol.*, **9**, 967 (2018).
9. A. Wilhelms *et al.*, Biodegradation of oil in uplifted basins prevented by deep-burial sterilization. *Nature* **411**, 1034-1037 (2001).
10. I. M. Head, D. M. Jones, S. R. Larter, Biological activity in the deep subsurface and the origin of heavy oil. *Nature* **426**, 344-352 (2003).
11. Materials and Methods are available as supplementary materials
12. B. Horsfield *et al.*, Living microbial ecosystems within the active zone of catagenesis: Implications for feeding the deep biosphere. *Earth Planet. Sci. Lett.* **246**, 55-69 (2006).
13. G. F. Moore, A. Taira, A. Klaus, and the Expedition 190 Scientists. *Proceedings of the Ocean Drilling Program, Initial reports*, **190**. (Ocean Drilling Program, College Station, Texas, 2001). doi:10.2973/odp.proc.ir.190.2001
14. V. B. Heuer, F. Inagaki, Y. Morono, Y. Kubo, L. Maeda, and the Expedition 370 Scientists. Temperature Limit of the Deep Biosphere off Muroto. *Proceedings of the International Ocean Discovery Program*. **370**, College Station, TX (International Ocean Discovery Program) (2017). <https://doi.org/10.14379/iodp.proc.370.101.2017>
15. M.-Y. Tsang *et al.*, Hot fluids, burial metamorphism and thermal histories in the underthrust sediments at IODP 370 Site C0023, Nankai Accretionary Complex. *Mar. Petr. Geol.* **112**, 104080 (2020).
16. T. Aüllo, A. Ranchou-Peyruse, B. Ollivier, M. Magot, Desulfotomaculum spp. and related gram-positive sulfate-reducing bacteria in deep subsurface environments. *Front. Microbiol.* **4**, 362 (2013).
17. C. Hubert *et al.*, A constant flux of diverse thermophilic bacteria into the cold Arctic seabed. *Science* **325**, 1541-1544 (2009).
18. S. Filippidou, T. Junier, T. Wunderlin, C. C. Lo, P. E. Li, P. S. Chain, P. Junier, Under-detection of endospore-forming Firmicutes in metagenomic data. *Comput. Struct. Biotechnol. J.* **13**, 299-306 (2015).
19. L. Wörmer *et al.*, Microbial dormancy in the marine subsurface: Global endospore abundance and response to burial. *Sci. Adv.* **5**, eaav1024 (2019).



20. A. R. Katritzky, A. R. Lapucha, M. Siskin, Aqueous high-temperature chemistry of carbo- and heterocycles. 3. 2-substituted pyridines. *Energy Fuels* **4**, 506-510 (1990).
21. J. Kallmeyer, A. Boetius, Effects of temperature and pressure on sulfate reduction and anaerobic oxidation of methane in hydrothermal sediments of Guaymas Basin. *Appl. Environ. Microbiol.*, **70**, 231-1233 (2004).
22. T. Holler *et al.*, Thermophilic anaerobic oxidation of methane by marine microbial consortia. *ISME J.* **5**, 1946-1956 (2011).
23. R. J. Parkes, B. A. Cragg, P. Wellsbury, P., Recent studies on bacterial populations and processes in seafloor sediments: a review. *Hydrogeol. J.*, **8**, 11-28 (2000).
24. P. Wellsbury *et al.*, Deep marine biosphere fuelled by increasing organic matter availability during burial and heating. *Nature* **388**, 573-576 (1997).
25. V. B. Heuer, J. W. Pohlman, M. E. Torres, M. Elvert, K.-U. Hinrichs, The stable carbon isotope biogeochemistry of acetate and other dissolved carbon species in deep seafloor sediments at the northern Cascadia Margin. *Geochim. Cosmochim. Acta* **73**, 3323-3336 (2009).
26. D. Govert, R. Conrad, Stable carbon isotope fractionation by acetotrophic sulfur-reducing bacteria. *FEMS Microbiol. Ecol.* **71**, 218-225 (2010).
27. S. H. Brown, R. M. Kelly, Cultivation techniques for hyperthermophilic archaeobacteria - continuous culture of *Pyrococcus Furiosus* at temperatures near 100-degrees-C. *Appl. Environ. Microbiol.* **55**, 2086-2088 (1989).
28. D. E. Canfield, K. S. Habicht, B. O. Thamdrup, The Archean sulfur cycle and the early history of atmospheric oxygen. *Science* **288**, 658-661 (2000).
29. F. Beulig, H. Roy, C. Glombitza, B. B. Jorgensen, Control on rate and pathway of anaerobic organic carbon degradation in the seabed. *Proc. Natl. Acad. Sci. U. S. A.* **115**, 367-372 (2018).
30. S. H. Zinder, M. Koch, Non-aceticlastic methanogenesis from acetate: acetate oxidation by a thermophilic syntrophic coculture. *Arch. Microbiol.* **138**, 263 - 272 (1984).
31. J. Kim *et al.* Naturally occurring, microbially induced smectite-to-illite reaction. *Geology* **47**, 535-539 (2019).
32. P. M. Fulton *et al.*, Low coseismic friction on the Tohoku-Oki Fault determined from temperature measurements. *Science* **342**, 1214-1217 (2013).
33. Y. Hamada *et al.*, In-situ mechanical weakness of subducting sediments beneath a plate boundary décollement in the Nankai Trough. *Progress in Earth and Planetary Science* **5**, 70 (2018).
34. M. E. Torres *et al.*, Crustal fluid and ash alteration impacts on the biosphere of Shikoku Basin sediments, Nankai Trough, Japan. *Geobiology* **13**, 562-580 (2015).

#### Supplementary Materials:

[www.sciencemag.org/content/###](http://www.sciencemag.org/content/###)

Materials and Methods and Supporting Text

Figs. S1 to S10

Tables S1 to S2

References (35–81)

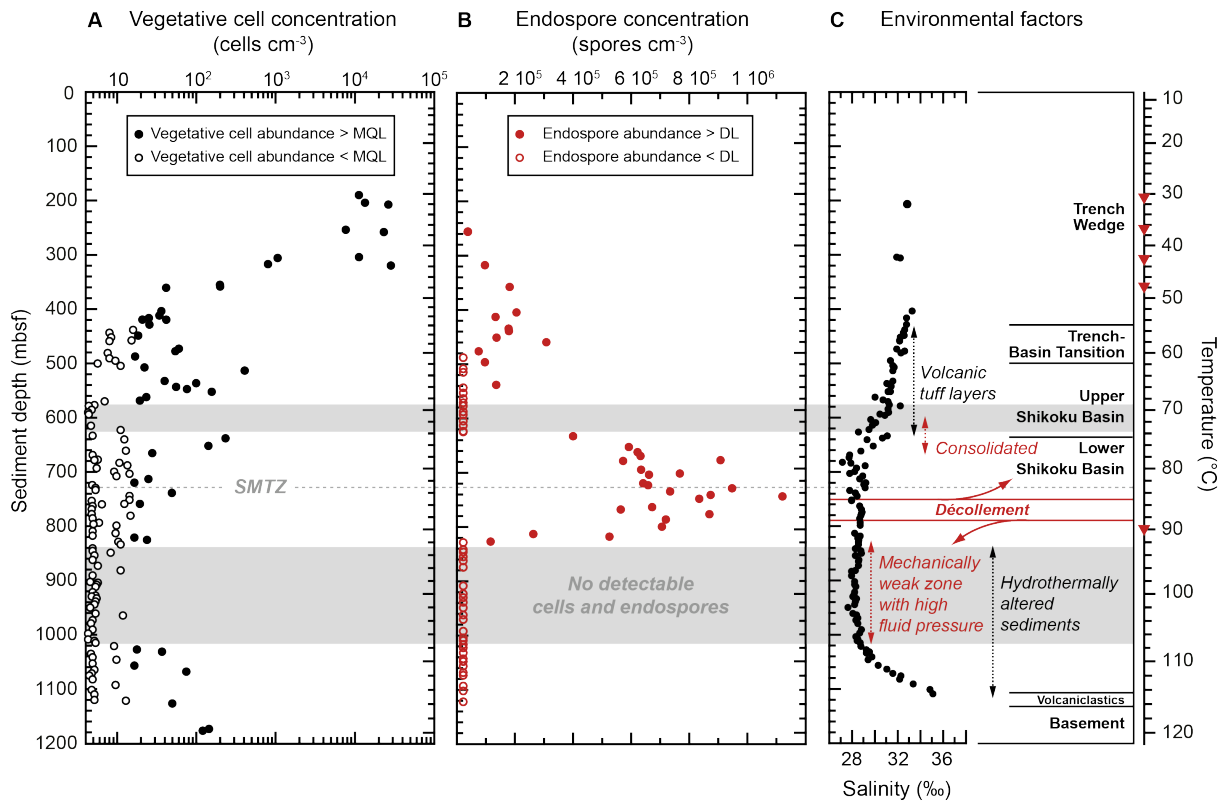


**Fig. 1. Depth profiles of vegetative cells and endospores in relation to environmental factors at IODP Site C0023.** (A) Concentrations of vegetative cells determined by counting of microbial cells fluorescently stained with SYBR Green I; based on a procedural blank of  $4.2 \pm 4.0$  cells  $\text{cm}^{-3}$  of sediment ( $N = 20$ ), the minimum quantification limit (MQL) was 16 cells  $\text{cm}^{-3}$ . (B) Concentrations of bacterial endospores derived from the diagnostic biomarker dipicolinic acid; analytical sensitivity corresponds to a detection limit (DL) of  $2.2 \times 10^4$  endospores  $\text{cm}^{-3}$ . (C) A schematic summary of environmental factors such as temperature, tectonic units, and salinity showing the geochemical influence of basalt alteration in the basement; red symbols on the temperature axis designate the depth horizons at which in-situ temperature measurements were made (11). Gray shading indicates zones where concentrations of both vegetative cells and endospores were below the detection limits of the employed methods in all investigated samples; SMTZ indicates the location of the sulfate-methane transition zone (cf. Fig. 2).

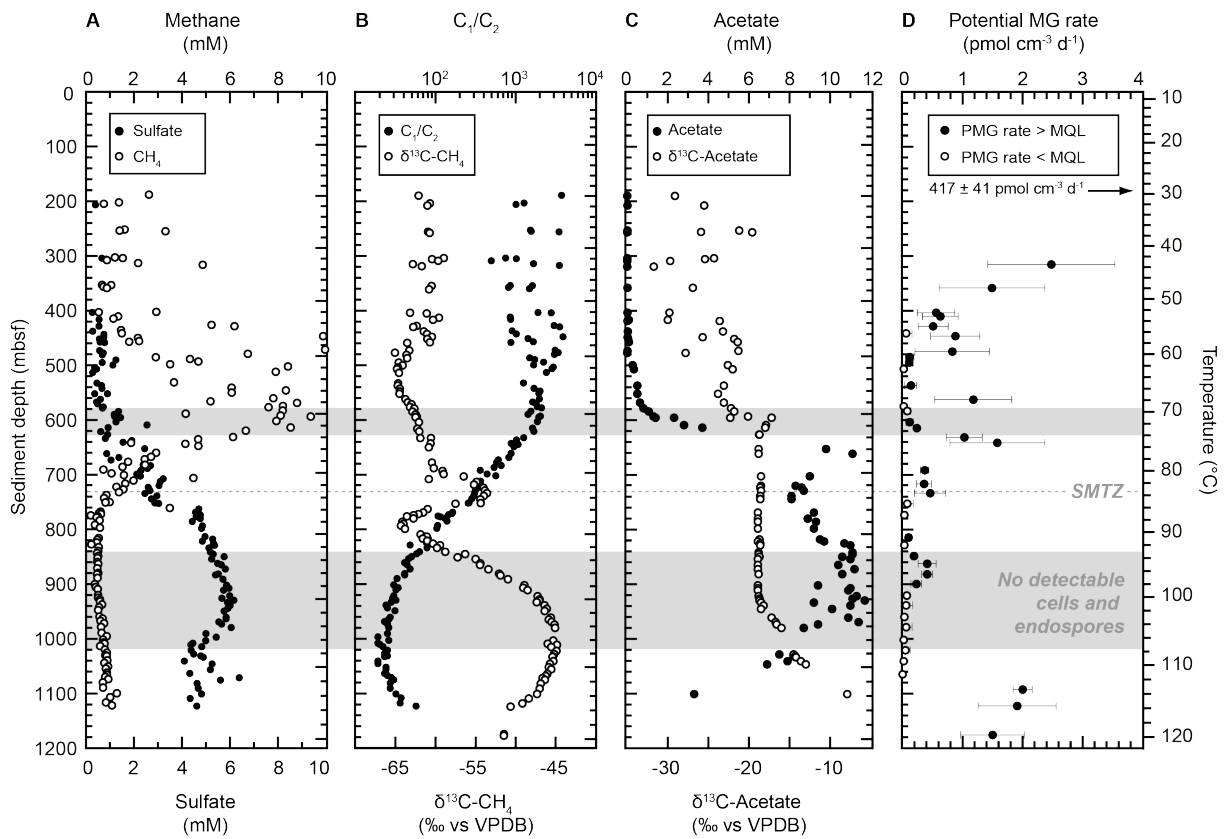


**Fig. 2. Geochemical signals of microbial metabolism at Site C0023.** (A) Dissolved methane (14) and sulfate (14), (B)  $C_1/C_2$  ratios (14) and  $\delta^{13}C-CH_4$ , (C) dissolved acetate and  $\delta^{13}C$ -acetate, and (D) potential rates of methanogenesis (MG) based on conversion of  $^{14}C-CO_2$  to  $^{14}C-CH_4$ ; note that the value at 180 mbsf lies off the scale off the chart. Potential MG (PMG) rates were determined at 40°C for  $\leq 360$  mbsf, 60°C for 405-585 mbsf, 80°C for 604-775 mbsf, and 95 °C for  $\geq 816$  mbsf. The minimum quantification limit (MQL) was 0.094 pmol  $CH_4 cm^{-3} d^{-1}$ . Gray shading, SMTZ and temperature axis are as in Fig. 1. VPDB in panels B and D is the Vienna Pee Dee Belemnite standard.

## Supplementary Materials for

### Temperature limits to deep seafloor life in the Nankai Trough subduction zone

V. B. Heuer,<sup>1\*</sup> F. Inagaki,<sup>2,3\*</sup> Y. Morono,<sup>3\*</sup> Y. Kubo,<sup>4,a</sup> A. J. Spivack,<sup>5</sup> B. Viehweger,<sup>1</sup> T. Treude,<sup>6</sup> F. Beulig,<sup>7,b</sup> F. Schubotz,<sup>1</sup> S. Tonai,<sup>8</sup> S. A. Bowden,<sup>9</sup> M. Cramm,<sup>10</sup> S. Henkel,<sup>11</sup> T. Hirose,<sup>3</sup> K. Homola,<sup>5</sup> T. Hoshino,<sup>3</sup> A. Ijiri,<sup>3</sup> H. Imachi,<sup>12</sup> N. Kamiya,<sup>13,c</sup> M. Kaneko,<sup>14</sup> L. Lagostina,<sup>15,d</sup> H. Manners,<sup>16</sup> H.-L. McClelland,<sup>17,e</sup> K. Metcalfe,<sup>18</sup> N. Okutsu,<sup>19,f</sup> D. Pan,<sup>20,g</sup> M. J. Raudsepp,<sup>21,h</sup> J. Sauvage,<sup>5,i</sup> M.-Y. Tsang,<sup>22</sup> D. T. Wang,<sup>23,j</sup> E. Whitaker,<sup>24</sup> Y. Yamamoto,<sup>25,k</sup> K. Yang,<sup>26,l</sup> L. Maeda,<sup>4</sup> R. R. Adhikari,<sup>1</sup> C. Glombitza,<sup>27</sup> Y. Hamada,<sup>3</sup> J. Kallmeyer,<sup>28</sup> J. Wendt,<sup>1</sup> L. Wörmer,<sup>1</sup> Y. Yamada,<sup>2</sup> M. Kinoshita,<sup>29</sup> K.-U. Hinrichs<sup>1§</sup>

\*V.B.H, F.I., and Y.M. contributed equally to this work.

§Corresponding author: E-mail: khinrichs@uni-bremen.de (K.-U.H.)

<sup>1</sup>Center for Marine Environmental Sciences (MARUM), University of Bremen, Bremen, Germany

<sup>2</sup>Research and Development Center for Ocean Drilling Science (ODS), Japan Agency for Marine-Earth Science and Technology, Yokohama, Japan

<sup>3</sup>Kochi Institute for Core Sample Research (KCC), Japan Agency for Marine-Earth Science and Technology, Kochi, Japan

<sup>4</sup>Center for Deep Earth Exploration (CDEX), Japan Agency for Marine-Earth Science and Technology, Yokohama, Japan

<sup>5</sup>Graduate School of Oceanography, University of Rhode Island, Narragansett, USA

<sup>6</sup>Department of Earth, Planetary, and Space Sciences, Department of Atmospheric and Oceanic Sciences, University of California, Los Angeles (UCLA), Los Angeles, USA

<sup>7</sup>Center for Geomicrobiology, Department of Bioscience, Aarhus University, Aarhus, Denmark

<sup>8</sup>Faculty of Science and Technology, Kochi University, Kochi, Japan

<sup>9</sup>Department of Geology and Petroleum Geology, School of Geosciences, University of Aberdeen, Aberdeen, United Kingdom

<sup>10</sup>Department of Biological Sciences, University of Calgary, Calgary, Canada

<sup>11</sup>Alfred Wegener Institute, Helmholtz Centre for Polar and Marine Research, Bremerhaven, Germany

<sup>12</sup>Institute for Extra-cutting-edge Science and Technology Avantgarde Research, Japan Agency for Marine-Earth Science and Technology, Yokosuka, Japan

<sup>13</sup>Graduate School of Integrated Basic Sciences, Nihon University, Tokyo, Japan

<sup>14</sup>Geomicrobiology Research Group, National Institute of Advanced Industrial Science and Technology (AIST), Tsukuba, Japan

<sup>15</sup>Department of Environmental Systems Science, ETH Zürich, Zürich, Switzerland

<sup>16</sup>School of Geography, Earth and Environmental Sciences, Faculty of Science and Engineering, Plymouth University, Plymouth, United Kingdom

<sup>17</sup>Department of Earth and Planetary Sciences, Washington University in St. Louis, St. Louis, USA

<sup>18</sup>Division of Geological and Planetary Sciences, California Institute of Technology, Pasadena, USA

<sup>19</sup>Atmosphere and Ocean Research Institute, University of Tokyo, Tokyo, Japan

<sup>20</sup>Department of Subsurface Geobiological Analysis and Research, Japan Agency for Marine-Earth Science and Technology, Yokosuka, Japan

<sup>21</sup>School of Earth Sciences, University of Queensland, St. Lucia, Australia

<sup>22</sup>Department of Earth Sciences, University of Toronto, Toronto, Canada

<sup>23</sup>Department of Earth, Atmospheric and Planetary Sciences, Massachusetts Institute of Technology, Cambridge, USA

<sup>24</sup>Department of Oceanography, Texas A&M University, College Station, USA

<sup>25</sup>Department of Mathematical Science and Advanced, Technology (MAT), Japan Agency for Marine-Earth Science and Technology, Yokosuka, Japan

<sup>26</sup>Department of Earth System Sciences, Yonsei University, Seoul, Republic of Korea

<sup>27</sup>Institute of Biogeochemistry and Pollutant Dynamics, ETH Zürich, Zürich, Switzerland

<sup>28</sup>Helmholtz Centre Potsdam, GFZ German Research Centre For Geosciences, Potsdam, Germany

<sup>29</sup>Earthquake Research Institute, University of Tokyo, Tokyo, Japan

Present address:

<sup>a</sup>Kochi Institute for Core Sample Research (KCC), Japan Agency for Marine-Earth Science and Technology, Kochi, Japan

<sup>b</sup>Department of Ecological Microbiology, University of Bayreuth, Bayreuth, Germany

<sup>c</sup>Graduate School of Engineering, Kyoto University, Kyoto, Japan

<sup>d</sup>Robert Koch-Institut, Berlin, Germany

<sup>e</sup>School of Earth Sciences, University of Melbourne, Melbourne, Australia

<sup>f</sup>Institute for Marine-Earth Exploration & Engineering, Japan Agency for Marine-Earth Science and Technology, Yokohama, Japan

<sup>g</sup>Department of Ecology & Environmental Studies, The Water School, Florida Gulf Coast University, Fort Myers, USA

<sup>h</sup>Department of Earth and Atmospheric Sciences, The University of Alberta, Edmonton, Canada

<sup>i</sup>Department of Marine Sciences, University of Gothenburg, Gothenburg, Sweden

<sup>j</sup>ExxonMobil, 22777 Springwoods Village Parkway, Spring, Texas 77389 USA

<sup>k</sup>Graduate School of Geoscience, Kobe University, Kobe, Japan

<sup>l</sup>Department of Oceanography, Pusan National University, Busan, Republic of Korea

**This pdf file includes**

Supporting information, incl. Material and Methods and supporting text

Figures S1 to S10

Tables S1 to S2

References 35-81

## 1 **Materials and Methods and Supporting Text**

### 2 *1. Study site and operations (fig. S1)*

3 This study aimed to elucidate the influence of temperature on microbial communities in deep  
4 seafloor sediments, and to determine the limits of microbial life. The particular challenge of such an  
5 endeavor arises from the necessity to potentially demonstrate the absence of microbial life. Accordingly,  
6 the highest possible levels of analytical sensitivity and contamination control need to be achieved under  
7 the demanding conditions of kilometer-deep scientific drilling. Expedition 370 of the International Ocean  
8 Discovery Program (IODP) was designed to meet this challenge. Our study site is located at the  
9 deformation front of the Nankai Trough subduction zone (fig. S1), ~125 km off Cape Muroto, Japan, in  
10 the vicinity of Sites 808 and 1174 of the Ocean Drilling Program (ODP) (35, 13). Due to high heat flow in  
11 this region (36), we expected to encounter the currently known upper temperature record of microbial  
12 life in the laboratory, ~120°C (5), at a relatively shallow depth of ~1.2 km below seafloor. From such  
13 depth, sediment cores can be retrieved by non-riser drilling, i.e. without the continuous circulation of  
14 dense drilling muds in a riser system, which is needed to advance to depths of several kilometers but  
15 associated with considerable contamination risks (3). At the same time, the increase of temperature with  
16 depth is still gradual enough to allow the observation of critical transitions with high depth and  
17 temperature resolution. For example, a 10°C change across the upper temperature limits of mesophiles  
18 (~43°C), thermophiles (~80°C), or deep seafloor life in general can be expected to stretch over a 100  
19 m depth interval in the borehole.

20 When Site C0023 (Hole C0023A: 32°22.00'N, 134°57.98'E, 4776 m water depth) was drilled and cored  
21 with *DV Chikyu* to a total depth of 1180 meters below seafloor (mbsf), sediment coring was combined  
22 with in-situ temperature measurements down to 408 mbsf. For greater depths, a precise temperature  
23 model was established based on detailed physical property measurements. Operations were concluded  
24 with the installation of a borehole observatory for long-term temperature measurements down to 860  
25 mbsf. No cores were retrieved from <189 mbsf, as the upper portion of the hole needed to be stabilized  
26 with a 20-inch casing. Cores of typically 3-9 m length were cut by a short advance modified hydraulic  
27 piston coring system (S-HPCS) from 189 mbsf to 408 mbsf, and by continuous rotary core barrel (RCB)  
28 coring from >410 mbsf to the bottom of the hole. Several measures were taken to minimize potential  
29 contamination and alteration of samples. (I) To avoid intrusion of microbes from drilling fluid during  
30 coring, intact parts of sediment cores without drilling induced fractures were identified by X-ray  
31 computed tomography (CT) image scans, sampled in the form of whole round cores (WRC) and cleaned  
32 immediately after retrieval. (II) To avoid introduction of microbes with airborne particles during sample  
33 processing in the laboratory, a super-clean working environment was established using tabletop air  
34 filtration units and static electricity neutralizers (ionizers) inside anaerobic chambers and clean benches.  
35 (III) To minimize alteration of depressurized samples and loss of information during storage, the carefully  
36 cleaned, anaerobically packed, refrigerated or frozen samples were transported by helicopter shuttle to  
37 Kochi Core Center (KCC) in Kochi Prefecture, Japan, on an almost daily basis. On shore, samples were  
38 further processed without delay in a laboratory that meets the International Organization for  
39 Standardization (ISO) Class 1 clean room standards. Operations at Site C0023 started with IODP  
40 Expedition 370 in September 2016 and finished with the retrieval of data from the temperature  
41 observatory and collection of surface sediments during *RV Kairei/ROV Kaiko* cruise KR18-04 in March  
42 2018. All operations, quality control measures, sampling procedures, shipboard analyses, and the  
43 installation and retrieval of the borehole observatory are described in detail in the expedition reports  
44 (14, 37).

45

46 *2. Geology, physical properties, and thermal history of Site C0023 (fig. S2)*

47 As part of the Philippine Sea Plate, Site C0023 has been approaching the trench from the Shikoku Basin  
48 at a rate of around 41-65 mm y<sup>-1</sup> for a total of ~16 million years (My). During the ~750 km long passage  
49 from spreading center to subduction zone, a 14 m thick layer of volcanoclastics and a 618 m thick layer of  
50 hemipelagic mudstone, occasionally interspersed by volcanic ash layers, piled up on the crust with an  
51 average sedimentation rate of ~35-53 m My<sup>-1</sup> (38). Upon arrival in the trench ~0.4 million years ago (Ma),  
52 sedimentation rates increased drastically to up to ~1319 m My<sup>-1</sup> (38). Since then, a 494 m thick layer of  
53 sand and silt rich mudstone accumulated, partly from debris flows or turbidity currents. The resulting  
54 succession of lithological units (fig. S2A) is consistent with previous findings (13, 35) and comprises axial  
55 trench-wedge facies (Subunit IIA, 189-318.5 mbsf), outer trench-wedge facies (Subunit IIB, 353-428  
56 mbsf), trench-to-basin transitional facies (Subunit IIC, 428-494 mbsf), upper Shikoku Basin facies (Unit III,  
57 494-637.25 mbsf), lower Shikoku Basin facies (Unit IV, 637.25-1112 mbsf), acidic volcanoclastics (Unit V,  
58 1112-1125.9 mbsf), and basaltic basement (Unit VI, 1125.9-1177 mbsf) (14). Both basin and trench  
59 deposits contain only little organic matter. Total organic carbon (TOC) contents decrease monotonically  
60 from 0.5 wt% at 190 mbsf to 0.02 wt% at the bottom of the hole, and low TOC/N ratios around 5.8 ± 2.1  
61 point to a predominantly marine source of the organic material (cf. Fig. F51 in ref. 14).

62 Site C0023 is located in the protothrust zone of the Nankai Accretionary prism, which has formed by the  
63 off-scraping of sediment from the descending Philippine Plate (39). Situated seaward from the frontal  
64 thrust, Site C0023 shows little deformation compared to the landward part of the prism, but detachment  
65 surfaces are present and bisect the succession of lithological units into three separate domains (fig. S2A),  
66 i.e., (I) an upper domain that comprises the prism, cut by low angle thrusts, (II) the décollement zone at  
67 758-796 mbsf, consisting of relatively thin, characteristically brecciated fault zones that are alternating  
68 with several meter thick intact zones, and (III) an underthrust domain with extensional faulting and no  
69 thrust fault zones (14).

70 The physical properties of Site C0023 are reflected in the down-hole profiles of porosity, *P*-wave velocity,  
71 and equivalent strength (EST) (fig. S2, ref. 14, 33). All three parameters show distinct deviations from a  
72 smooth compaction curve. (I) Porosities, inferred from moisture and density measurements of discrete  
73 sediment and rock samples (fig. S2B), generally decrease with increasing depth from 40% to 50% at 200  
74 mbsf to 32% at 1030 mbsf. However, a distinct reversal of this trend occurs across and below the  
75 décollement, where porosities increase by 5-7% (760-830 mbsf). In contrast, porosities decrease more  
76 sharply than expected in mud rocks and volcanoclastics at the bottom of the hole (>1030 mbsf). In the  
77 underlying basaltic basement rocks, porosities range from 5.5% to 25%. (II) *P*-wave velocity stands for  
78 the speed at which ultrasonic sound waves pass through a material, and it is related not only to the  
79 material's porosity but also to its compressibility and shear strength. At Site C0023, *P*-wave velocities,  
80 measured on intact sediment cores, reflect the general down-hole decrease of porosity as well as its  
81 excursion towards higher porosities across the décollement and the sharp decrease of porosities in  
82 sediments and basaltic rocks at the bottom of the hole (fig. S2C). At ~630 mbsf, however, elevated *P*-  
83 wave velocities do not match the high porosities of bulk sediment samples (45-50%). This finding points  
84 to a stiffening of the fine to coarse tuff and tuffaceous muds in this interval, potentially due to diagenetic  
85 mineral alteration reactions (40). (III) EST is a measure for the in-situ strength of the geological  
86 formation, i.e. its relative triaxial shear strength that can be deduced from parameters recorded during  
87 the drilling operation, such as weight-on-bit, top drive torque, and rotations per minute (33). The down-

88 hole EST profile of Site C0023 (fig. S2D, ref. 33) shows distinctly elevated mechanical strength for the  
89 tuff-rich sediments around ~630 mbsf, as well as the presence of a mechanically weak zone below the  
90 décollement, stretching from ~800-1050 mbsf. In this zone, EST decreases by a factor of 5 from 10 to 2  
91 MPa. While the mechanical weakening is clearly evident in the EST profiles, which has been measured  
92 under in-situ pressure conditions, there is no corresponding decrease in the down-hole *P*-wave velocity  
93 profile, which has been generated on core samples after pore pressure had been released during  
94 recovery. The deviation between EST and *P*-wave velocity suggests that the mechanical weakness of the  
95 upper portion of the underthrust domain is related to high in-situ pore pressure. If pore pressure  
96 exceeds hydrostatic pressure, the effective pressure on sediments is reduced and consequently their in-  
97 situ strength decreases. Together, the physical properties of Site C0023 suggest that (a) volcanoclastic  
98 sediments in the prism domain form a distinct, mechanically strong layer ~630 mbsf, (b) the upper 250 m  
99 of the underthrust domain (~800-1050 mbsf) are under-compacted and mechanically weak due to the  
100 presence of overpressurized fluids, and (c) the décollement (758-796 mbsf) forms a barrier that does not  
101 allow fluids to flow from the underthrust sediments into the prism domain.

102 These observations agree well with previous studies, which infer the presence of high-fluid pressure  
103 below the décollement from seismic imaging (41, 42), suggest the possibility that a décollement acts as a  
104 barrier inhibiting upward fluid convection, leading to high pore pressure and increased structural  
105 weakness of subducting sediments (43-45), and explain the surplus of water below the décollement with  
106 in-situ dehydration of clay minerals (46, 47) and/or channelized lateral advective fluid flow from deeper  
107 portions (48, 49).

108 At Site C0023, signs of low-temperature hydrothermal mineralization provide evidence for fluid flow in  
109 the underthrust domain (14, 15). Between 775 and 1121 mbsf, hydrothermal mineralization assemblages  
110 occur in the form of veins and stratabound alteration patches, which are rich in barite and  
111 rhodochrosite, pale-yellow in color, and often 10-15 cm thick (14). Due to their elevated density,  
112 hydrothermal minerals are visible in X-ray CT images, and consequently their down-hole distribution can  
113 be tracked by radiodensity logging, as shown in fig. S2E (cf. ref. 50). For the known hydrostatic pressures  
114 and modern concentrations of dissolved barium within the underthrust sediments of Site C0023,  
115 retrograde solubility for barite would occur above 145°C (15). Analyses of fluid inclusions in authigenic  
116 barite minerals revealed high salinities of around 16-25% NaCl equivalent and trapping temperatures  
117 ranging from 118-141°C at 822 mbsf to 146-219°C at 1010 mbsf (15). These salinities and  
118 homogenization temperatures distinctly exceed present-day salinities and temperatures at Site C0023,  
119 and point to mixing with deep-sourced hot and saline fluids (15). The morphology of the authigenic  
120 minerals in veins and burrows suggest that the ingress of such fluids started before and continued  
121 throughout the deformation of underthrust sediments (15). Tsang et al. (15) estimate the duration of  
122 individual hydrothermal fluid flow events by fitting a heat flow model, which predicts the spatial and  
123 temporal expansion of thermal aureoles along permeable sedimentary fabrics, to the actual size of  
124 hydrothermal veins and alteration patches observed by visual core description and radiodensity logging  
125 (14, 50). They conclude that the ingress of hydrothermal fluids has occurred in the form of episodic  
126 short-term pulses, which have lasted for less than three days and altered sediment temperatures within  
127 up to 30 cm thick aureols around veins or alteration patches (15). Hydrothermal mineral assemblages  
128 were found down to 1121 mbsf (14, 15). Their absence at greater depths points to a lack of  
129 hydrothermal influence in the oldest sediments of Site C0023. Instead, hematized sediments and  
130 reddening occur in both sediments and basalts at the sediment/basalt interface together with low-  
131 temperature mineral assemblages such as calcite veins that penetrate both crust and sediment (14, 15).



132 The close spatial association is typical for umbers, i.e. ferruginous horizons adjacent to oceanic basement  
133 that are associated with the end of rifting and low-temperature off-axis activity (15).

134 The episodic ingression of hydrothermal fluids has no measurable effect with respect to petroleum  
135 generation (15). Instead, the current thermal maturity of sedimentary organic matter at Site C0023 can  
136 solely be explained by conventional burial diagenesis (15). Three thermal maturity parameters, which  
137 were calculated from hopane and sterane biomarkers, indicate a thermal regime in which catagenesis  
138 has just begun, but the thermal state of Site C0023 can only be explained if past heat flows were higher  
139 than today (15). Biomarker and present-day temperature data agree best with a basin modeling  
140 scenario, in which heat flow was distinctly elevated 2 Ma, and formations in underthrust sediments  
141 began to cool about 0.1 Ma (15). Against the tectonic background of southeast Japan, a conceivable  
142 scenario for Site C0023 includes high heat flow close to the spreading center until 15 Ma, a subsequent  
143 transition through lower off-axis heat flows, and a brief increase in past heat flow around 2 Ma due to  
144 the far-field effect of increased volcanic activity (15). This scenario is consistent with a previous thermal  
145 history model for adjacent ODP Site 1174 (12).

146 Sediment temperature is a function of heat flow, thermal conductivity and depth below seafloor.  
147 Consequently, the arrival of Site C0023 in the trench ~0.4 Ma and the associated ~30-fold increase in  
148 sedimentation rates (38) led to a rapid ~50°C increase of temperature across the entire sediment  
149 column.

150

### 151 3. Modern temperature regime of Site C0023 (fig. S3-S4)

152 In order to determine the modern temperature regime of Site C0023, formation temperatures were  
153 measured in situ from 189.3 to 407.6 mbsf during drilling (14). Based on the deduced heat flow and  
154 thermal conductivities measured on samples, a temperature profile to the bottom of Hole C0023A was  
155 synthesized with the assumption of purely vertical conductive and steady-state heat flow (fig. S3). The  
156 projected downhole temperature reaches ~86°C at the top of the décollement zone and  $119.7 \pm 3.4^\circ\text{C}$  at  
157 the bottom of the hole (fig. S4). Post-cruise monitoring of temperatures in the borehole observatory  
158 confirm the projected temperatures and thus verify our temperature model (37).

#### 159 3.1 Overview of Method

160 We calculated the in-situ temperature profile based on the step-wise integration of Fourier's Law,

$$161 \quad q = -\kappa(z) \frac{dT(z)}{dz} \quad (1)$$

162 which gives,

$$163 \quad T(z) = T(z_0) - q \sum_{i=0}^N \left( \frac{\Delta z_i}{\kappa(z)_i} \right), \quad (2)$$

164 where,

165  $T(z)$  = temperature,

166  $z$  = depth from the sediment–bottom water interface,

167  $\kappa(z)$  = thermal conductivity,

168  $\Delta z_i$  = difference in depth between successive measurements of  $\kappa(z)$

169  $T(z_0)$  = temperature at the depth of first measurement,  $z_0$ ,

170  $q$  = heat flow, (note that in this coordinate system  $q < 0$ )

171  $\sum_{i=0}^N \left( \frac{\Delta z_i}{k(z)_i} \right)$  = thermal resistance, and

172  $N$  = number of thermal conductivity measurements (51).

173 Application of equation 2 requires an estimate of the heat flow and a profile of thermal conductivities.

174 Its use also assumes that heat flow is conductive, and is constant with depth as well as time. We

175 measured thermal conductivities with high spatial resolution, nearly one measurement per core down to

176 the basement ( $N = 111$ ) (14). The assumption of constant heat flow with depth may not be correct,

177 however. When the sediment accumulation rate is high and the column length is long, as potentially is

178 the case in the Nankai Trough, conduction may not keep pace with the burial of cold sediment and heat

179 flow can vary with depth.

180 To test the assumption of steady-state heat flow with depth and time at Site C0023, we first solve the

181 time-dependent heat flow equation, taking  $\kappa$ ,  $\rho$ , and  $C_p$  as depth independent

$$182 \quad \frac{\partial T(z,t)}{\partial t} = \frac{\kappa}{\rho C_p} \frac{\partial^2 T(z,t)}{\partial z^2} \quad (3)$$

183 where

184  $\rho$  = bulk sediment density and

185  $C_p$  = bulk sediment specific heat.

186 The solution of equation 3 for a sediment column whose length continuously increases due to sediment

187 accumulation and with constant basement heat flow is,

$$188 \quad T(z) = T(z_0) + \frac{\alpha^{1/2} L^{1/2} \pi^{1/2} \left( \frac{dT}{dz} \right)_{\text{measured}} e^{\eta'^2}}{s^{1/2}} (\text{erf}(\eta) - \text{erf}(\eta_L)) \quad (4)$$

189 where we used the Buckingham  $\pi$  theorem (52) to define the non-dimensional variable,  $\eta$ ,

$$190 \quad \eta = \frac{(L-z)s^{1/2}}{2\alpha^{1/2} L^{1/2}} \quad (5)$$

191 with

192  $\alpha$  = thermal diffusivity,  $\kappa/(\rho C_p)$ ,

193  $s$  = linear sediment accumulation rate,

194  $L$  = sediment column length, and

195  $\eta'$  = value of  $\eta$  at the depth the temperature gradient is measured

196  $\eta_L$  = value of  $\eta$  at depth  $z = L$ , the sediment-basement interface.

197 We then compare the solution of equation 1 (constant heat flux and assuming constant  $\kappa$ ) to the time

198 dependent solution, equation 4, to determine the temperature error offset,  $\Delta T(z=L) = T(z=L)_{\text{steady-}}$

199  $\text{state} - T(z=L)_{\text{time-dependent}}$ , that results from assuming steady-state heat flow. At the bottom of the

200 sediment column, the temperature offset,  $\Delta T(z=L)$ , of these two solutions is approximately given by:

$$201 \quad \Delta T(z = L) \approx \frac{-\left( \frac{dT}{dz} \right)_{\text{measured}} e^{\eta'^2} L^2 s}{12\alpha} \quad (6)$$

202 To get this estimate we expanded equation 4 as a Taylor series, keeping the first two terms, and then  
203 subtracted the steady-state solution, equation 3.

204 At Site C0023, the magnitude of  $\Delta T(z=L)$  is  $-1.0^\circ\text{C}$  based on the following typical values,

205  $(dT/dz)_{\text{measured}} = 0.1 \text{ (}^\circ\text{C m}^{-1}\text{)},$

206  $L\text{-}z$  for depth of temperature gradient measurement = 950 (mbsf),

207  $L = 1176 \text{ (m)},$

208  $s = 3.8 \cdot 10^{-11} \text{ (m s}^{-1}\text{)},$

209  $\rho = 2.0 \cdot 10^3 \text{ (kg m}^{-3}\text{) and}$

210  $C_p = 1.4 \cdot 10^3 \text{ (J kg}^{-1} \text{ }^\circ\text{C}^{-1}\text{)}.$

211 This is an upper limit of the offset as the sediment accumulation rate was more than an order of  
212 magnitude lower than assumed here during the accumulation of about half of the sediment column. This  
213 offset is within the error of measurement uncertainty ( $3.4^\circ\text{C}$ , see below), justifying the conductive  
214 steady-state assumption.

### 215 *3.2 Measurements at Site C0023*

216 Details of the methods for measuring temperature and thermal conductivity are given in refs. 14 and 53.  
217 Briefly, temperature was measured in-situ using a short advance modified hydraulic piston coring system  
218 (S-HPCS) equipped with an advanced piston corer temperature tool (APCT-3) until the S-HPCS could no  
219 longer penetrate properly into the formation (14). The APCT-3 consists of a thermistor that is  
220 hydraulically stroked up to 4.5 m into the sediment, well beyond the thermal influence of drilling  
221 operations. After penetration, it takes  $\sim 10$  min for the sensor to equilibrate to the in-situ temperature of  
222 the formation. Measured temperatures were extrapolated from the APCT-3 measurements, using the  
223 program TP-Fit (53). The uncertainty of individual measurements is estimated to be  $0.1\text{-}0.2^\circ\text{C}$  (e.g., ref.  
224 54).

225 Thermal conductivity was measured on sediment and rock samples using either the full-space needle  
226 probe or the half-space line source depending on sediment strength; the methods are described in detail  
227 in the expedition report (14). Values of thermal conductivity are based on the observed rise in  
228 temperature for a given quantity of heat. The full-space needle and the half-space line probes were  
229 calibrated at least once every 24 h. The calibration was performed on Macor samples of known thermal  
230 conductivity ( $1.611 \pm 2\% \text{ W m}^{-1} \text{ K}^{-1}$  and  $1.652 \pm 2\% \text{ W m}^{-1} \text{ K}^{-1}$  for the full- and half-space probes,  
231 respectively). We base the uncertainty of the entire method,  $\sim 2\%$ , on the variance of the measured data  
232 from a smooth fit.

233 Eight formation temperatures were measured in-situ between 189.3 to 407.6 mbsf. Based on quality  
234 assessment of coring and time series temperature data while measuring, we used four temperature data  
235 among the eight to determine the thermal gradient and heat flow. Temperatures increased linearly as a  
236 function of thermal resistance,  $\sum_{i=0}^N \left( \frac{\Delta z_i}{k(z)_i} \right)$  between 204.1 and 355.2 mbsf (fig. S3). In the temperature  
237 calculations, the value of  $k(z)_i$  is taken as the average of the two values measured at adjacent depths.  
238 The calculated heat flow, based on a linear least square of temperature vs. thermal resistance is  $-0.140$   
239  $\text{W m}^{-2}$  with a 90% confidence of  $\pm 0.005 \text{ W m}^{-2}$ . The uncertainty in the heat flow is consistent with the  
240 expected uncertainties in individual temperature measurements of  $\sim 0.1$  to  $0.2^\circ\text{C}$ .

241 Estimated temperatures are shown in fig. S4. The estimated temperature at the bottom of Hole C0023A  
242 (1176.6 mbsf) is  $119.7 \pm 3.4^\circ\text{C}$  (90% confidence limit).

243 The confidence limit is based on propagating the errors associated with the heat flow and thermal  
244 resistance. The uncertainty in the calculated temperature is dominated by the uncertainty in the heat  
245 flow (> 90% of the uncertainty). Uncertainty in thermal conductivity is minor due to the large number of  
246 measurements.

247

#### 248 *4. Cell concentrations (Fig. 1A)*

249 Enumeration of microbial cells in subsurface environments that are situated close to the limits of  
250 habitability requires the highest possible levels of analytical sensitivity and contamination control (55). In  
251 order to improve the detection limit of cell enumeration, microbial cells were detached from the  
252 sediment matrix by ultrasonication, subsequently recovered by density gradient centrifugation and  
253 concentrated on polycarbonate membrane filters, before they were treated with the nucleic acid stain  
254 SYBR Green I, and manually counted under the microscope. For maximal contamination control, we  
255 implemented rigorous quality assurance (QA) and quality control (QC) measures for all steps involved in  
256 core recovery, core processing, and sample analysis. Numerous cell counts in the range of the procedural  
257 blank (fig. S6) and negligible drilling disturbance (fig. S7) testify to the effectiveness of contamination  
258 control during sample handling. Detailed information on analytical methods and QA/QC procedures and  
259 results are given in the expedition report (14).

#### 260 *4.1 Cell enumeration*

261 In principle, sediment samples for cell enumeration were taken from the very center of selected, quality  
262 controlled WRCs under anoxic and sterile conditions, using sterilized spatulas or cut-off syringes in  
263 unconsolidated sediments and a table-top mini-drill in consolidated sediments. In consolidated  
264 sediments, the sterilized drill bit of the mini-drill was exchanged after each sample. Soft sediments were  
265 immediately submerged in fixation solution. Consolidated sediments were kept under anoxic conditions  
266 until they were crushed by ceramic pestle and mortar and immersed in fixation solution. Approximately  
267  $10\text{ cm}^3$  of powdered sediment were thoroughly mixed with fixation solution consisting of 20 mL of 3%  
268 (w/v) sodium chloride and 10% (v/v) neutralized formalin (containing 3.8% formaldehyde). If necessary,  
269 the mixture was stored at  $4^\circ\text{C}$ .

270 Fixed cells were separated from the slurry via ultrasonication and density gradient centrifugation (56).  
271 For cell detachment, a 1 mL aliquot of the formalin-fixed sediment slurry was amended with 1.4 mL of  
272 2.5% NaCl, 300  $\mu\text{L}$  of pure methanol, and 300  $\mu\text{L}$  of detergent mix (ref. 57, 100 mM ethylenediamine  
273 tetraacetic acid [EDTA], 100 mM sodium pyrophosphate, 1% [v/v] Tween-80). The mixture was  
274 thoroughly shaken for 60 min (Shake Master, Bio Medical Science, Japan), and subsequently sonicated at  
275 160 W for 30 s for 10 cycles (Bioruptor UCD-250HSA; Cosmo Bio, Japan). The detached cells were  
276 recovered by centrifugation based on the density difference of microbial cells and sediment particles,  
277 which allows collection of microbial cells in a low-density layer. To this end, the sample was transferred  
278 onto a set of four density layers composed of 30% Nycodenz ( $1.15\text{ g cm}^{-3}$ ), 50% Nycodenz ( $1.25\text{ g cm}^{-3}$ ),  
279 80% Nycodenz ( $1.42\text{ g cm}^{-3}$ ), and 67% sodium polytungstate ( $2.08\text{ g cm}^{-3}$ ). Cells and sediment particles  
280 were separated by centrifugation at  $10,000 \times g$  for 1 h at  $25^\circ\text{C}$ . The light density layer was collected using  
281 a 20G needle syringe. The heavy fraction, including precipitated sediment particles, was resuspended  
282 with 5 mL of 2.5% NaCl, and centrifuged at  $5000 \times g$  for 15 min at  $25^\circ\text{C}$ . The supernatant was combined

283 with the previously recovered light density fraction. With the remaining sediment pellet, the density  
284 separation was repeated. The sediment was resuspended using 2.1 mL of 2.5% NaCl, 300 µL of methanol,  
285 and 300 µL of detergent mix and shaken at 500 rpm for 60 min at 25°C, before the slurry sample was  
286 transferred into a fresh centrifugation tube where it was layered onto another density gradient and  
287 separated by centrifugation just as before. The light density layer was collected using a 20G needle  
288 syringe, and combined with the previously collected light density fraction and supernatant to form a  
289 single suspension for cell counting.

290 For cell enumeration, a 50%-aliquot of the collected cell suspension was passed through a 0.22-µm  
291 polycarbonate membrane filter. Cells on the membrane filter were treated with SYBR Green I nucleic  
292 acid staining solution (1/40 of the stock concentration of SYBR Green I diluted in Tris-EDTA [TE] buffer).  
293 The number of SYBR Green I-stained cells were enumerated by direct microscopic count (4, 58). At least  
294 900 fields of view were analyzed for each whole membrane filter.

295 The cell staining with DNA-staining dye, including SYBR Green I, critically relies on the penetration of dye  
296 into the cells. For normal “cells”, including subseafloor microbes, the staining has worked reliably and  
297 contributed to the exploration of the deep subseafloor biosphere (3). However, we found that the  
298 situation is different in endospores as they do not allow DNA-dyes to penetrate inside and are resistant  
299 to DNA-staining. The example in fig. S5 shows the staining of vegetative cells (fig. S5a) and endospores  
300 (fig. S5b) of *Bacillus subtilis* NBRC13719. Although the stainability was 100% in vegetative cells, 98.8%  
301 (N = 4707) spores appeared in orange color in fluorescence observation, which indicated the adsorption  
302 and overaccumulation of SYBR Green I on the surface of endospores (58). The adsorption was also  
303 indicated by the enlarged image of the orange-stained endospores, in which the center of the endospore  
304 remained black (i.e. unstained), while the center of the green-stained endospore was well-stained (fig.  
305 S5a). In addition, the staining and observation of endospores mixed with sterilized sediment  
306 demonstrated the extreme difficulty in identifying spores even for the cultivated species (fig. S5c). These  
307 results are consistent with the previous findings according to which endospore abundance assessed by  
308 the chemical quantification of dipicolinic acid exceeded the abundance of cells detected by DNA-  
309 staining-based direct counts in subseafloor sediments (18, 59). Moreover, the stainability of endospores  
310 inhabiting the subseafloor environment is expected to be substantially lower than that of cultivated  
311 spores of *B. subtilis* (1.2%). Therefore, we operationally call the SYBR-stainable cells as “vegetative cells”  
312 in this study.

#### 313 4.2 Quality assurance and quality control (QA/QC)

314 QA/QC measures were designed to account for three major sources of contamination during sample  
315 recovery and processing, namely introduction of microbial cells from drilling fluid, from airborne  
316 particles, and from reagents and tools used during sample processing.

317 *Intrusion of seawater and drilling mud during core cutting and recovery* - To minimize the risk of drilling-  
318 induced contamination, samples for microbiological investigations were taken as intact WRCs from the  
319 pristine, undisturbed parts of the recovered cores. Generally, the upper section of a core was not  
320 sampled to avoid cross contamination from loose borehole materials accumulating on the bottom of the  
321 hole. Undisturbed core intervals were identified based on visual inspection and X-ray CT imaging, which  
322 reveals the structural integrity of sediment cores on a sub-millimeter scale. All surfaces of WRCs, which  
323 had potentially been in contact with drilling fluid, were removed immediately after core retrieval  
324 onboard *DV Chikyu* to prevent diffusion of potential contaminants from seawater and drilling fluid into  
325 the inner part of the core during storage and transport. WRCs were opened in an anaerobic chamber,

326 where core liners were removed and all sediment surfaces were scraped off with sterile ceramic knives,  
327 before the remaining sediment cores were placed into ESCAL bags and temporarily sealed shut. The bags  
328 were removed from the anaerobic chamber, immediately flushed with nitrogen gas to remove H<sub>2</sub> gas,  
329 vacuum-sealed, and stored at +4°C. Afterwards, samples were transferred to shore by helicopter in order  
330 to enable prompt processing under clean-room conditions at KCC (see below). On shore, the scraping of  
331 WRC surfaces was repeated to further reduce the contamination risk, and samples for cell enumeration  
332 (~10 cm<sup>3</sup>) were taken from the very center of the WRCs.

333 X-ray CT-imaging not only allows one to identify and to avoid core intervals with fractures prone to  
334 contamination, it also enables quantification of core integrity and thus contamination risk for each  
335 selected sample (50). Using automated image and data processing routines, pristine, high-quality areas  
336 can be distinguished from damaged areas based on the characteristic values and distribution patterns of  
337 radiodensity in each 0.625 mm thick slice image recorded as a DICOM file during X-ray CT scanning. The  
338 resulting slice quality (SQ) is a quantitative measure for the relative abundance of drilling induced  
339 fractures in a given slice, with a SQ of 100% indicating the highest possible quality of a slice without any  
340 fractures. SQ has been shown to be an effective quality control measure, and automatic identification  
341 and removal of slices below a given SQ threshold generates quality-controlled downhole radiodensity  
342 profiles closely reflecting geological features (50). A detailed description and evaluation of this new  
343 method and its application during Expedition 370 are given in ref. 50.

344 During Expedition 370, we determined SQ for all 0.625 mm thick CT slices of the typically ~5-40 cm long  
345 WRC samples selected for cell enumeration, and used the resulting mean slice quality of all CT slices  
346 (mean SQ) as a measure for the core quality of an individual cell count sample. This quantitative  
347 evaluation shows that careful, X-ray CT guided sample selection achieved the highest possible core  
348 quality, i.e. a mean SQ of 100%, in 46% of all WRCs taken for cell enumeration. The prevalence of  
349 excellent core quality in all cell count samples is evident in a typical mean SQ of 99% (median of 152  
350 samples, fig. S6A).

351 In addition, established routines for contamination testing were applied to monitor the potential  
352 intrusion of drilling fluid into the cores through the use of a chemical tracer (14). In the main pump room  
353 of *DV Chikyu*, the perfluorocarbon (PFC) tracer perfluoromethylcyclohexane was added to the down-  
354 going drilling fluid. After its proper delivery was verified by analysis of drilling fluid captured inside the  
355 core liners, the intrusion of PFC into the core was monitored in ~2 cm<sup>3</sup> sediment samples taken from the  
356 exterior, midway, and interior portions of WRCs. During operations, pumping rates and mixing ratios of  
357 drilling mud varied in response to borehole conditions. Consequently, the exact concentration of PFC in  
358 the down-going drilling fluid remains unknown. In order to assess the potential drilling induced  
359 contamination without this information, we determined PFC recovery. PFC recovery normalizes the PFC  
360 concentration measured in the center part of an individual core to the average PFC concentration in the  
361 outer parts of all cores ( $0.22 \pm 0.81 \mu\text{g cm}^{-3}$ , N = 74), which had been in direct contact with drilling fluid. A  
362 PFC recovery of 0% in the core center represents the lowest risk of drilling induced contamination.  
363 During Expedition 370, PFC recovery was <1% in the majority of samples taken from the interior portions  
364 of WRCs, and the lack of relation between PFC recovery and vegetative cell abundance suggest that  
365 drilling induced contamination is negligible in the high-quality intervals of the sediment cores, which  
366 were selected for microbiological samples (fig. S6B).

367 *Contamination of sediment samples from airborne particles during laboratory work* – In order to avoid  
368 introduction of airborne particles, all sample processing was conducted under clean-room conditions.

369 Cleaning and subsampling of WRCs, both onboard *DV Chikyu* and at KCC, were conducted inside  
370 anaerobic chambers (95:5 [v/v] N<sub>2</sub>:H<sub>2</sub> atmosphere; COY Laboratory Products, USA) equipped with a  
371 KOACH T 500-F tabletop air filtration unit (Koken, Ltd. Japan) and a Winstat air ionizer BF-X2MB  
372 (Shinshido Electrostatic Ltd., Japan). The air filtration unit circulates the limited volume of gas inside the  
373 anaerobic chamber quickly, and effectively removes dust particles generated during sample processing.  
374 In this manner, clean air conditions are established that are comparable to the air quality in ISO Class 1  
375 clean environments. The ionizer neutralizes surface charge and reduces static attraction of potentially  
376 contaminating airborne particles. Subsampling yielded a compact subcore (2 cm diameter) that was  
377 aseptically drilled out of the center of the WRCs. All further processing steps, including crushing of  
378 samples into powder, cell separation and filtration were conducted in a super-clean room at KCC. The  
379 super-clean room is equipped with a Floor KOACH Ez that produces horizontal ISO Class 1 quality of  
380 laminar airflow from the end wall of the clean space (60). All of the clean experiments were conducted  
381 upstream, in front of the KOACH clean units, and electronic equipment (centrifuges, refrigerator, and  
382 sonicator) was placed downstream of the clean space. To neutralize the static electricity of the samples,  
383 plastic equipment, and gloves (hands), a bar-type sheath-sensing ionizer (SJ-H180, Keyence, Japan) was  
384 placed approximately 40 cm above the working area of the stainless steel laboratory bench, and the  
385 static elimination capacity was routinely checked with high-precision electrostatic sensors (SK-H055 and  
386 SK-J050, Keyence, Japan) (14).

387 The presence of airborne particles in the laboratory air of *DV Chikyu*, in the anaerobic chambers, and in  
388 the super-clean room at KCC was monitored throughout the expedition (14). In the shipboard and shore-  
389 based workspaces, the concentration of airborne particles was recorded with a Met One HHPC 3+  
390 airborne particle counter (Met One Instruments, Inc.; Grants Pass, Oregon, USA) and with a Biotest  
391 particle counter (9303-01BT), respectively. Particle concentrations were determined for three particle  
392 size classes (>0.3, >0.5, >1 μm). In the shipboard and shore-based anaerobic chambers, particle counts  
393 were reduced by up to five orders of magnitude compared to the surrounding laboratory air, and  
394 airborne particle concentrations in the vicinity of the work area of the super-clean room at KCC were  
395 consistently below the detection limit of the particle counter (<1 particle ft<sup>-3</sup>) (14).

396 To quantify the concentration of airborne microbial cells that may potentially contaminate cores during  
397 shipboard core handling, cells in 1 L of air were counted from the various workspaces. To this end, 1 L of  
398 air was drawn through a 0.22-μm polycarbonate membrane in a syringe filter housing (Swinnex Filter  
399 Holder, 25 mm, Merck Millipore). Cells on the filter were preserved with formaldehyde fixation solution,  
400 treated with SYBR Green I nucleic acid staining solution, and enumerated as described above. Visual  
401 inspection of the membranes under the microscope revealed submicrometer-scale particle densities  
402 consistent with particle counts in all core processing workspaces. However, in the anaerobic chambers  
403 and in the super-clean room at KCC, none of these particles were cells. Overall, our QA/QC measures  
404 reduced airborne particle contamination to negligible levels.

405 *Introduction of microbial cells and chemical compounds from equipment and chemicals used during*  
406 *sample processing* - During the cutting of cores and processing of samples, sediment came only in  
407 contact with precleaned (with 18 MΩ water) and sterilized tools, such as autoclaved spatulas and  
408 ceramic knives, or precombusted (500°C for 5 h) ceramic pestles and mortars. Tools were replaced  
409 whenever potential contamination by contact with a nonsterile surface was suspected. WRCs were  
410 packed with end caps that had been cleaned with ethanol, dried in a clean bench, and irradiated with UV  
411 light for at least 20 min prior to use. Interior surfaces of the anaerobic chamber were routinely  
412 decontaminated by wiping with RNase AWAY (Thermo Fisher Scientific). In addition, the working surface

413 was covered with a fresh sheet of precombusted aluminum foil (500°C for 5 h) each time a new WRC was  
414 processed. The N<sub>2</sub> gas used to store samples under anoxic, H<sub>2</sub>-free conditions was filtered with a 0.22-μm  
415 filter to remove potential contamination.

416 In order to quantify the remaining contamination risk from reagents, tools and airborne particles, 20  
417 negative controls were included into the sample preparation line at KCC. Negative control membranes  
418 were prepared by passing saline solution through all cell separation and membrane preparation  
419 protocols. On eight out of the 20 negative control membranes, no cells were found in 900 fields of view.  
420 The other 12 controls contained up to 3 cells in 900 fields of view. Considering the ratio of reagents used  
421 per sediment sample, the analytical blank of cell enumeration was  $4.2 \pm 4.0$  cells cm<sup>-3</sup> (N = 20). Based on  
422 this analytical contamination risk, the abundance of microbial cells in sediment samples can be reliably  
423 determined above a minimum quantification limit (MQL) of 16 cells cm<sup>-3</sup> of sediment (95% confidence  
424 level).

#### 425 *4.3 Remaining contamination risks during Expedition 370 (figs. S6, S7)*

426 Expedition 370 achieved an unprecedented level of sensitivity for life detection, yet cell concentrations  
427 fall below the MQL in 70% of all 138 samples recovered from >350 m depth. The numerous cell counts in  
428 the range of the procedural blank testify to the effectiveness of contamination control during sample  
429 handling. Most strikingly, cell concentrations average  $6.0 \pm 3.1$  cells cm<sup>-3</sup> in 32 consecutively taken  
430 samples from the zone between 829 and 1020 mbsf (fig. S6). These samples reflect 21 events for the  
431 cutting and retrieval of sediment cores from Hole C0023A by rotary core barrel (RCB) coring, and 32  
432 events for the selection, cutting, and processing of WRCs in the shipboard laboratories. In all these  
433 samples, cell concentrations do not differ significantly from the procedural blank of  $4.2 \pm 4.0$  cells cm<sup>-3</sup> (N  
434 = 20). This observation again suggests that the implemented QA/QC measures reduced the introduction  
435 of microbial cells via drilling fluid and shipboard handling to a negligible level.

436 Against this background, elevated cell counts in 30% of the samples recovered from >350 m depth call  
437 for a rigorous examination of the remaining contamination risks, such as intrusion of drilling fluids into  
438 sediment cores along natural and drilling-induced fractures. Quantification of core integrity by X-ray CT-  
439 imaging does not only confirm the excellent quality of all cell count samples (see above), it also allows  
440 for a quantitative comparison of core quality and cell concentrations in all WRCs taken from Hole  
441 C0023A. Fig. S7A suggests that cell abundances are not related to the amount of fractures in the sampled  
442 core intervals. While  $\leq 16$  cells cm<sup>-3</sup> were counted in eight samples taken from WRCs with a mean SQ of  
443 only 74-90%, 11 out of 34 samples with the highest possible core quality, characterized by a mean SQ of  
444 100%, yielded vegetative cell counts above the MQL. Cell abundances are not correlated with core  
445 quality (Spearman correlation  $\rho = -0.0095$ ,  $p$  (2-tailed) = 0.929). Consequently, elevated cell counts  
446 cannot be attributed to drilling induced contamination along fractures. This conclusion is further  
447 supported by the lacking relationship between vegetative cell abundance and PFC recovery, which  
448 represents the potential contamination of sediment cores by drilling fluid via advection and diffusion (fig.  
449 S7B).

450

#### 451 *5. Endospores*

452 Endospores are a dormant form of some members of the bacterial order Firmicutes. Endospores may  
453 survive under harsh conditions over geological timescales. Endospores contain the bacterial DNA,  
454 ribosomes and large amounts of dipicolinic acid (DPA). In contrast to vegetative cells, endospores cannot



455 be visualized with DNA-staining dyes such as SYBR Green I (fig. S5), and thus escape microscopic cell  
456 counting methods. We therefore used the biomarker DPA to determine the abundance of endospores in  
457 the sediments of Site C0023. To facilitate a quantitative comparison of endospores and vegetative cells,  
458 DPA concentrations were converted into endospore numbers per cm<sup>3</sup> of wet sediment. Average  
459 concentrations of endospores and vegetative cells were integrated over four depth intervals (table S1),  
460 and the relationship between concentrations of endospores and vegetative cells was examined in a  
461 temporal framework considering the geothermal history of Site C0023 with the help of a mathematical  
462 model.

### 463 *5.1. Determination of sedimentary dipicolinic acid (DPA) and endospore concentration (Fig. 1B)*

464 Sampling for DPA analysis and cell counting were closely coordinated and guided by X-ray CT imaging  
465 and visual core inspection as described above. In total, 78 WRCs were collected for DPA analysis from  
466 Site C0023. The cored sediment remained inside the core liners after cutting, and each WRC was packed  
467 in a sterile plastic bag and additionally secured in an aluminum bag. Both bags were immediately flushed  
468 with N<sub>2</sub> and vacuum-sealed, before the sediment cores were frozen with a Cells Alive System freezer  
469 (CAS, ref. 61) and stored at -20°C until further treatment.

470 For post-cruise DPA analysis, a ~4-5 cm thick disk of sediment was cut from each frozen WRC, and the  
471 outer 5-mm layer was removed by scraping, using a flame sterilized chisel. Samples were freeze dried  
472 and stored at -20°C. For extraction, a 15-mL polypropylene tube was filled with ~1 g of freeze-dried,  
473 homogenized sediment. 4 mL of Tris buffer (0.2 M; pH = 7.6) was added, because it maximizes the  
474 extraction yield in clayey sediments. After vortexing, samples were autoclaved for 20 min at 121°C to  
475 extract DPA. After cooling down, 80 µL of 2 mM AlCl<sub>3</sub> solution was added to precipitate phosphates,  
476 which might otherwise quench the fluorescence signal. Tubes were centrifuged for 10 min at 3000 rpm,  
477 then supernatants were collected, filtered through 0.2-µm cellulose-acetate filters (Chromafil CA-20/15  
478 MS) and stored at -20°C until analysis. Each WRC was extracted in duplicate, and one replicate was  
479 spiked with 200 nM DPA as an internal standard to allow for quantification. WRCs were processed in  
480 random order. Each batch for extraction included eight WRC samples, and two procedural blanks.

481 For analysis, 600 µL of each sample extract were evaporated to dryness at 50°C under a N<sub>2</sub> stream and  
482 afterwards dissolved in 120 µL of a 500 mM NaHSO<sub>4</sub> solution (pH = 1.2). Detection of DPA closely  
483 followed the method described by Fichtel et al. (62, 63) using reverse phase high performance liquid  
484 chromatography (HPLC) with fluorescence detection. We employed a Phenomenex Gemini 3-µm C18  
485 column (150 x 2 mm) and a Thermo FLD-3400 RS detector. 100 µL of each sample were injected to a  
486 mobile phase consisting of 50 mM NaHSO<sub>4</sub> (pH = 1.2) and acetonitrile (97:3) delivered at a flow rate of  
487 0.5 mL min<sup>-1</sup>. After 10 min, a 3-min gradient to 65:35 was applied, followed by stable conditions for 1  
488 min, and a reset to initial conditions within 0.5 min. The system was re-equilibrated for 4 min before the  
489 next injection. Fluorescence detection of DPA was achieved by supplying TbCl<sub>3</sub> (50 µM) post-column via a  
490 secondary pump at a flow rate of 0.1 mL min<sup>-1</sup> (for further details see ref. 64). DPA was identified based  
491 on its characteristic fluorescence (emission at 543 nm after excitation at 271 nm) and retention time.

492 Quantification of DPA was achieved by comparing the integrated peak area of DPA in the unspiked  
493 sample to the difference of peak areas between the spiked and unspiked sample, which corresponds to a  
494 concentration of 200 nM DPA. DPA abundances were normalized to sediment mass and transferred to  
495 endospore concentrations using the empirically determined conversion factor of 2.24 x 10<sup>-16</sup> mol DPA per  
496 endospore (64). Each plotted data point represents the mean of duplicate samples. Standard deviations  
497 average around 18% of the reported mean value.

498 Sediment dry weight (dw) endospore concentrations were converted to volumetric concentrations by  
499 multiplying endospores  $\text{g}^{-1}$  dw with a grain density of  $2.7 \text{ g cm}^{-3}$  (range of  $2.68 \text{ g cm}^{-3}$  at 250 mbsf to  $2.79$   
500  $\text{g cm}^{-3}$  at 1100 mbsf, cf. Fig. 39B in ref. 14) and then multiplied by (1-porosity) of the sample closest in  
501 depth to the endospore sample (MAD data, cf. T06 and T07 in ref. 14).

502 The detection limit was  $2.2 \times 10^4$  endospores  $\text{cm}^{-3}$ . It was defined as the DPA concentration measured in  
503 representative sediment samples with a signal-to-noise ratio of 3. The corresponding peak area equaled  
504 a DPA concentration of  $3.1 \times 10^{-3}$  nmol DPA  $\text{g}^{-1}$  dry weight and was converted to endospores  $\text{g}^{-1}$  dw and  
505 endospores  $\text{cm}^{-3}$  wet weight as described for the samples. For the determination of the detection limit,  
506 transformation to wet weight was based on porosity value of 0.58 from the middle of the core (604.8  
507 mbsf).

## 508 *5.2 Ratio of endospores relative to vegetative cells (table S1)*

509 In order to determine ratios of endospores to vegetative cells for selected depth intervals of interest,  
510 average concentrations of endospores and vegetative cells for these intervals needed to be determined.  
511 Average concentration values representative of defined depth intervals (cf. table S1) for both variables  
512 were determined by the sum of all integrals between available measurement depths, divided by the  
513 length of the depth interval of interest. The upper interval boundary was either 250 mbsf or 350 mbsf,  
514 i.e., the approximate depth of the uppermost subsurface sample analyzed for endospores and the  
515 approximate depth after the major decline of vegetative cell concentrations (cf. Fig. 1). The lower  
516 interval boundary was either 1177 mbsf (sediment/basement boundary; endospore data were  
517 extrapolated below 1121 mbsf) or 1121 mbsf (lowest endospore sample). In cases in which no cells or no  
518 endospores were detected, we used the analytical blank value of  $4.2 \pm 4.0$  cells  $\text{cm}^{-3}$  for vegetative cells  
519 and the detection limit of  $2.2 \times 10^4$   $\text{cm}^{-3}$  for endospores. As this relatively high detection limit for  
520 endospores could introduce some artificially high endospore to cell ratios, we also computed an  
521 alternative value by setting concentrations in samples with no detection to 4 endospores  $\text{cm}^{-3}$ , equal to  
522 the analytical blank of the vegetative cell data. As shown in table S1, differences between both  
523 approaches are minor.

## 524 *5.3 Assessing the significance of the two major endospore peaks in relation to low concentrations of* 525 *vegetative cells (fig. S8)*

526 The two major endospore peaks centered around  $\sim 400$  and  $\sim 650$  mbsf are prominent features and raise  
527 the question of how they developed in the geological context of Site C0023. Moreover, the orders of  
528 magnitude lower concentrations of vegetative cells relative to endospores and the fact that endospore-  
529 forming firmicutes commonly account for only a relatively small fraction of the microbial population (65-  
530 69), call for explanatory scenarios in which the vegetative microbial population has been larger and/or  
531 more active in the recent past, at least intermittently. While the elucidation of the exact mechanism  
532 leading to the observed predominance of endospores in deeply buried sediments at Site C0023 goes  
533 beyond the scope of this study, the observation of the two major endospore peaks nevertheless calls for  
534 an examination of their plausibility and significance.

535 We rule out that the molecular endospore biomarker DPA accumulated throughout the depositional  
536 history, based on its propensity as 2-carboxylated pyridine to decarboxylate upon moderate short-term  
537 heating (19). Moreover, it is striking that the position of the two peaks coincide with the upper growth  
538 temperatures of mesophiles and thermophiles, suggesting a biological rather than geochemical cause.  
539 We therefore constructed a simple quantitative model that explores the accumulation of the observed

540 quantities of endospores at Site C0023. For both endospore peaks, we consider as major mechanism  
541 triggering sporulation the relatively rapid heating of the sediment column initiated ~0.4 Ma by the  
542 drastic increase of sediment accumulation rate (38).

543 For the shallower peak the increase of sediment temperatures to the upper growth temperature of  
544 mesophilic firmicutes provides a conceivable trigger of sporulation. Such a scenario is consistent with the  
545 concomitant decrease of vegetative cells in the same sediment horizon (cf. Fig. 1). For the second, larger  
546 peak, scenarios starting from current concentration levels of vegetative cells, of which only 1-10% may  
547 be endospore-forming Firmicutes (cf. 65-67) or even less (68, 69), appear implausible unless we invoke  
548 past events leading to exponential growth and rapid increase of the population of vegetative cells,  
549 followed by sporulation and decay of this population. While we cannot categorically rule out such a  
550 possibility, it seems inconsistent with the general characteristic of energy starvation encountered by  
551 deeply buried microbial communities as well as the geological setting of the horizon, in which no obvious  
552 triggers of rapid exponential growth are apparent.

553 Due to the absence of reasonable triggers of exponential growth linked to the stratigraphy, we therefore  
554 consider a mechanism based on the assumption that a background population of thermophilic  
555 endospores (17), too low in size to be detected by our DPA-based biomarker approach, is present in  
556 deeply buried sediments. The feasibility of a corresponding mechanism explaining the quantitative  
557 relationship between endospores and vegetative cells at Site C0023 is explored in figure S8; the  
558 underlying model assumes that the above-mentioned background population of endospores germinates  
559 upon the onset of accelerated geothermal heating of the sediments to form vegetative cells. The  
560 widespread presence of thermophilic endospores has been suggested based on the observation that in  
561 Arctic sediments, thermophilic sulfate-reducing bacterial communities can be activated upon heating of  
562 the sediments to the growth temperature range of thermophiles (17). Persistence of thermophilic  
563 endospores on million-year timescales is also plausible, according to laboratory experiments (70) and  
564 provided that temperatures are not excessively high. We consider that temperatures of 50-75°C  
565 represent the ideal growth range for thermophilic, anaerobic endospore formers, and thus explore the  
566 development of the populations of vegetative cells and endospores upon heating of the sediment to  
567 50°C (fig. S8). This temperature may have been reached about 0.32 Ma in the sediment interval of 633-  
568 827 mbsf, representing the more deeply buried endospore peak.

569 Our model assumes the presence of a background population of 1000 thermophilic endospores cm<sup>-3</sup> (red  
570 dashed line; this value is lower than estimated background populations in young Arctic surface  
571 sediments (17) and was arbitrarily chosen to be lower than our detection limit) and initial germination of  
572 vegetative Firmicutes from these endospores at 0.32 Ma, when temperatures reached 50°C; subsequent  
573 growth of the Firmicutes populations lasted for 0.2 My until sediment temperatures in this horizon had  
574 reached 75°C.

575 Accordingly, we can estimate the concentration of vegetative cells ( $C_n$ ) and the corresponding  
576 concentration of endospores for the  $n^{\text{th}}$  generation ( $S_n$ ) with equations 7 and 8, respectively. From initial  
577 germination of the background population of endospores after reaching 50°C, we assume  $C_0$  of 10<sup>3</sup> cm<sup>-3</sup>  
578 and  $S_0$  of 0 cm<sup>-3</sup>. We further assume that in each generation, 49% of the cells sporulate and 51% double  
579 by cell division. This corresponds to a 2% increase in population size per generation. The sporulation rate  
580 of 49% was chosen to keep concentrations of vegetative cells as low as possible throughout the  
581 examined time interval, in accordance with the generally low current concentrations of vegetative cells.

582 
$$C_n = 0.51 \times C_{n-1} \times 2 \quad (7)$$

583 
$$S_n = S_{n-1} + 0.49 \times C_{n-1} \times 2 \quad (8)$$

584 
$$T_d = \frac{2 \times 10^5}{n} \quad (9)$$

585 Growth was halted at 75°C, as this is the upper growth limit for most thermophilic Firmicutes (71), and  
586 likewise coincides with the in-situ temperature of the major endospore peak (Fig. 1). This model does  
587 not account for the decay of vegetative cells; incorporation of cell decay into the model would  
588 consequently increase the number of required generations and lower the generation time. In line with  
589 the DPA derived endospore data (Fig. 1), we assume endospore concentrations above 75°C to remain  
590 roughly constant until they rapidly decline at temperatures above 90°C.

591 With this approach, 156 generations were required to arrive at a final concentration  $S_{156}$  of  $>1 \times 10^6$   
592 endospores within 0.2 My, corresponding to a doubling time  $T_d$  of 1290 years (equation 9); the  
593 corresponding population of vegetative Firmicutes is  $2 \times 10^4$  cells  $\text{cm}^{-3}$ . This modeled final and maximal  
594 concentration is higher than the  $<10^3$  cells  $\text{cm}^{-3}$  observed in the modern-day 50 to 75°C warm interval;  
595 potential reasons include the selection of our model parameters and/or varying concentrations of  
596 background endospore input through the sedimentation history and/or different sedimentary conditions  
597 between the 400-650 mbsf interval corresponding to the Upper Shikoku Basin and the modern  
598 endospore peak within the Lower Shikoku Basin.

599

## 600 6. Geochemical evidence for microbial activity (Fig. 2)

601 Sediment pore-water profiles of microbial substrates, intermediates, and products provide insights into  
602 *in-situ* microbial activity and integrate a variety of processes in time and space. In this study, we present  
603 concentration profiles of sulfate, methane, and acetate together with the carbon isotopic composition  
604 ( $\delta^{13}\text{C}$ ) of methane ( $\delta^{13}\text{C}\text{-CH}_4$ ) and acetate ( $\delta^{13}\text{C}\text{-acetate}$ ) (Fig. 2). We compare the relative abundance of  
605 methane and ethane (expressed as ratio of methane over ethane,  $C_1/C_2$ ) as indicator of biogenic vs.  
606 thermogenic methane sources (Fig. 2). Moreover, we calculate Gibbs free energy yields for various  
607 reactions involving methane and acetate, and we employ a diffusion-reaction model for the  
608 interpretation of changes in the carbon isotopic composition of pore-water acetate. In the following, we  
609 provide details on sampling, analytical methods, and our modeling approach.

### 610 6.1 Sampling

611 Shipboard and shore-based gas analyses were conducted on sediment samples that were taken from the  
612 freshly cut core and allowed to degas dissolved gases into the headspace of a tightly closed glass vial  
613 (head space sampling) (14). For shipboard analysis of light hydrocarbon gases ( $C_1\text{-}C_4$ ),  $\sim 5 \text{ cm}^3$  of sediment  
614 were transferred into 20 mL headspace vials, which were immediately sealed with a silicone septum and  
615 metal crimp cap. For shore-based analysis of  $\delta^{13}\text{C}\text{-CH}_4$ ,  $\sim 5 \text{ cm}^3$  of sediment were transferred into 20 mL  
616 headspace vials, and preserved with 5 mL of 1 N NaOH solution before the vials were sealed with butyl  
617 stoppers and crimp caps. Samples were stored at  $-20^\circ\text{C}$ .

618 Pore-water sulfate and acetate were analyzed in interstitial water samples extracted from 10 to 80 cm  
619 long WRCs, which were cut from core sections with minimal drilling disturbance, selected as described in  
620 the expedition report (14) and above (cf. section 4.2). Sediment was extruded from the core liners and  
621 prepared for squeezing in a nitrogen-flooded glove bag in order to minimize the oxidation of oxygen-  
622 sensitive species. The outer layer of the sediment cores was carefully removed with a ceramic knife to

623 avoid contamination from drilling fluid, and the cleaned sediment was filled into the titanium beakers of  
624 the squeezer. Interstitial water was then extracted using a Carver laboratory hydraulic press, which was  
625 not in the glove bag. In general, a force up to 30,000 lb was applied. This maximum force was chosen to  
626 avoid clay mineral dehydration. However, the force was increased to up to 60,000 lb for a few samples  
627 that did not yield sufficient water (reported in Table T13 of the expedition report [14]). The interstitial  
628 water was passed through an Advantec 13 100% alpha cotton cellulose 3- $\mu\text{m}$  filter inside the squeezer  
629 (both prewashed with 18 M $\Omega$  water), collected in a 24-mL acid-washed plastic syringe, extruded through  
630 a Millipore Millex-LH hydrophilic 0.45- $\mu\text{m}$  polytetrafluoroethylene (PTFE) disposable filter and collected  
631 into acid-washed high-density polyethylene (HDPE) vials. For shipboard sulfate analysis, an aliquot of the  
632 interstitial water samples was diluted 1:200 with 18.2 M $\Omega$  deionized water. Samples for shore-based  
633 analysis of acetate were stored in pre-combusted glass vials at -20°C. All sampling procedures are  
634 described in detail in the expedition report (14).

635 In the course of the expedition, QA/QC routines revealed a variance in dissolved sulfate concentrations  
636 that, based on a diffusion model, could be attributed to the diffusion of sulfate from the core liner fluid  
637 into the core. The scatter in sulfate concentrations decreased when thicker layers were removed from  
638 the outer surface of sediment cores prior to squeezing. While initially the outer ~3 mm were scraped off  
639 from each sediment surface, 5 mm and finally 7 mm were removed after Core 54R (712.71 mbsf) and  
640 Core 83 R (864.88 mbsf), respectively.

## 641 6.2 Analytical methods

642 *Methane and higher hydrocarbons* – For shipboard analysis of concentrations of methane and higher  
643 hydrocarbon gases (C<sub>2</sub>-C<sub>4</sub>), the headspace vials were placed in an Agilent Technologies 7697A headspace  
644 sampler, where they were heated to 70°C for 30 min before an aliquot of the headspace gas was  
645 automatically injected into an Agilent 7890B GC equipped with a packed column (HP PLOT-Q) and flame  
646 ionization detector (FID). He was the carrier gas (10 cm<sup>3</sup> min<sup>-1</sup>). After injection, the initial column oven  
647 temperature of 60°C was ramped at a rate of 10°C min<sup>-1</sup> to 150°C. Chromatographic response of the FID  
648 was calibrated with commercial standards, and the response of the FID was checked on a daily basis as  
649 described in the expedition report (14). Based on the analyzed partial pressures of methane in  
650 headspace gas samples, the concentrations of dissolved pore-water methane were derived using a mass  
651 balance approach (14). The resulting hydrocarbon gas data are reported in Table T21 and T22 of the  
652 expedition report (14).

653 *Sulfate* – Shipboard analysis of sulfate was conducted using a Dionex ICS-2100 ion chromatograph. The  
654 column oven was set at 30°C. The eluent solution was 40 mM potassium hydroxide. Aliquots of a  
655 standard (IAPSO Batch 157, salinity = 34.994) were used in all analytical batches. In each batch, every  
656 diluted sample was analyzed twice. Variations due to temperature-dependent changes in the injected  
657 volume and sample dilution were corrected by normalization to chloride, which was determined  
658 independently by titration. An IAPSO standard was analyzed after every fifth analysis for drift correction,  
659 thus yielding an uncertainty of 0.02 mM for sulfate analysis. All methods and raw data are documented  
660 in detail in the expedition report (14, Table T14 in ref. 14).

661  $\delta^{13}\text{C}-\text{CH}_4$  – The carbon isotopic composition of methane was analyzed on shore by isotope ratio  
662 monitoring gas chromatography/mass spectrometry (irm-GC/MS), using a Thermo Finnigan Trace GC  
663 Ultra connected to a Thermo Finnigan DELTA Plus XP mass spectrometer via a Thermo Finnigan GC  
664 combustion III interface. The Trace GC was equipped with a Carboxen column (30 m length, 0.32 mm  
665 inner diameter). The carrier gas was helium (3 mL min<sup>-1</sup>), the split ratio ranged from 1:3 to 1:100

666 depending on sample concentration, and the temperatures of the GC oven and injector were 40°C and  
667 200°C, respectively. The primary standardization was based on multiple injections of reference CO<sub>2</sub> from  
668 a lab tank ( $\delta^{13}\text{C} = -34.17 \pm 0.1\text{‰}$  vs. VPDB,  $3.0 \pm 0.5 \text{ V}$  at  $m/z$  44) at the beginning and end of the analysis  
669 of each sample. The analytical precision was better than 0.4‰ (1 $\sigma$ ).

670 *Acetate and  $\delta^{13}\text{C}$ -acetate* - Concentration and carbon isotopic composition of acetate were analyzed on  
671 shore by isotope ratio monitoring high performance liquid chromatography/mass spectrometry (irm-  
672 HPLC/MS) as described previously (25). The analysis involves chromatographic separation of VFAs on a  
673 Thermo Finnigan Surveyor HPLC combined with chemical oxidation of the effluents in a Thermo Finnigan  
674 LC IsoLink interface and subsequent online transfer of the resulting CO<sub>2</sub> into a Thermo Finnigan DELTA  
675 Plus XP mass spectrometer via open split. Chromatographic separation was achieved with a VA 300/7.8  
676 Nucleogel Sugar 810H column (300 mm length; 7.8 mm ID; Macherey-Nagel) equipped with a guard  
677 column (CC30/4 Nucleogel Sugar 810H; 30 mm length; Macherey-Nagel), and 5 mM phosphoric acid as  
678 mobile phase with a flow rate of 300  $\mu\text{L min}^{-1}$ . The column was kept at room temperature. The  
679 quantitative analysis of VFAs is based on the linear correlation between signal area of  $m/z$  44 recorded  
680 by irm-LC/MS and injected amount of carbon (72). For carbon isotope analysis of VFAs, primary  
681 standardization on the DELTA Plus XP is based on multiple (three to six) injections of reference CO<sub>2</sub> ( $\delta^{13}\text{C}$   
682 =  $-34.3 \pm 0.1\text{‰}$  vs. VPDB,  $3.5 \pm 0.5 \text{ V}$  at  $m/z$  44) from a tank before and after the analysis of each sample.  
683 We calculated the  $^{13}\text{C}/^{12}\text{C}$  ratios of the eluting compounds and the corresponding  $\delta^{13}\text{C}$ -values according  
684 to Ricci et al. (73) and Santrock et al. (74), using ion currents of  $m/z$  44 and  $m/z$  45 integrated over time  
685 for each individual peak and a mean  $^{17}\text{O}/^{16}\text{O}$  ratio for each chromatographic run that resulted from the  
686 analysis of the CO<sub>2</sub> reference peaks. Precision and accuracy were assessed by periodic analysis of  
687 standards as described previously (72). Standard deviations for repeated carbon isotope analysis were  
688 <0.6‰, and mean  $\delta^{13}\text{C}$  values of dissolved VFAs deviated by <0.6‰ from those determined for their salts  
689 by elemental analyzer/isotope ratio mass spectrometer (EA/IRMS). The detection limit for carbon  
690 isotope analysis of acetate was 10  $\mu\text{M}$ , i.e. slightly higher than the detection limit of 5  $\mu\text{M}$  for  
691 quantitative acetate analysis. Samples with acetate concentrations exceeding 1.3 mM were diluted 1:10  
692 with MilliQ water to facilitate accurate analysis.

### 693 6.3 Thermodynamic calculations (Fig. S9)

694 The standard Gibbs energy ( $\Delta G^0_{\text{insitu}}$ ) of sulfate-dependent AOM ( $\text{CH}_4 + \text{SO}_4^{2-} \rightarrow \text{HCO}_3^- + \text{HS}^- + \text{H}_2\text{O}$ ),  
695 sulfate reduction from acetate ( $\text{SO}_4^{2-} + \text{CH}_3\text{COO}^- \rightarrow \text{HS}^- + 2\text{HCO}_3^-$ ), sulfate reduction from hydrogen ( $4\text{H}_2 +$   
696  $\text{SO}_4^{2-} + \text{H}^+ \rightarrow \text{HS}^- + 4\text{H}_2\text{O}$ ), methanogenesis from acetate ( $\text{CH}_3\text{COO}^- + \text{H}_2\text{O} \rightarrow \text{CH}_4 + \text{HCO}_3^-$ ), and  
697 methanogenesis from hydrogen ( $4\text{H}_2 + \text{HCO}_3^- + \text{H}^+ \rightarrow \text{CH}_4 + 3\text{H}_2\text{O}$ ) (fig. S9) was calculated using the  
698 SUPCRT/OBIGT software package (75) and reported thermodynamic data (76-78) for in-situ  
699 temperatures estimated from the local geothermal gradient (fig. S4) and a median pressure of 55.8 MPa.  
700 The energy of reactions at non-standard conditions ( $\Delta G_R$ ) was calculated according to:

$$701 \quad \Delta G_R = \Delta G^0_{\text{insitu}} + R \times T \times \ln Q \quad (10)$$

702 where  $R$  (0.008314  $\text{kJ mol}^{-1} \text{K}^{-1}$ ) is the ideal gas constant,  $T$  (in K) is the *in-situ* temperature, and  $Q$   
703 denotes the activity quotient of the reactants and reaction products. Activities were estimated by  
704 multiplying the measured concentration of the species with activity coefficients calculated from an  
705 extended version of the Debye-Hückel equation (79) for an ionic strength of  $I = 0.64$  and in-situ  
706 temperatures using the Geochemists Workbench<sup>®</sup> Software (www.gwb.com). In depths where  $\text{HS}^-$  was  
707 below detection, we assumed a molar concentration of 0.1  $\mu\text{mol L}^{-1}$ .

708 6.4  $\delta^{13}\text{C}$ -acetate diffusion-reaction model (Fig. S10)

709 Profiles of concentrations of acetate and its carbon isotopic compositions ( $\delta^{13}\text{C}$ -acetate) (Fig. 2C) indicate  
710 effective turnover of acetate in up to 60°C hot sediments, minimal utilization of acetate between 60°C  
711 and 100°C, and the presence of a biological acetate sink above 100°C. Dissolved acetate concentrations  
712 ([Ac]) are sub-millimolar in sediments of the Upper Shikoku Basin and increase at the transition to the  
713 Lower Shikoku Basin where they remain relatively constant, at  $9.2 \pm 2.4$  mM (Fig. 2). Starting near the  
714 Upper and Lower Shikoku Basin interface,  $\delta^{13}\text{C}$ -acetate is invariable,  $-18.8 \pm 0.5\%$ , within the  
715 measurement precision (0.6‰) (Fig. 2C). This constancy breaks at the transition between the zone of no  
716 detectable microbial cells and the deep cell-populated zone. Acetate concentrations decrease while  $\delta^{13}\text{C}$ -  
717 acetate monotonically increases with depth, reaching a maximum measured value of  $-7.9\%$  at 1101  
718 mbsf. This combination of isotope and concentration data implies catabolic acetate utilization.

719 The interval of invariable  $\delta^{13}\text{C}$ -values is consistent with production of acetate from isotopically  
720 monotonous organic matter, by thermal degradation and possibly fermentation. In contrast, the deep  
721 increase of  $\delta^{13}\text{C}$ -values is consistent with biological utilization of acetate, which favors the  $^{13}\text{C}$ -depleted  
722 acetate isotopologue, leaving the unreacted acetate enriched in  $^{13}\text{C}$  (25, 72, 80). At any depth, the  
723 isotopic composition of acetate reflects the composition of the source(s), the isotopic fractionation  
724 associated with consumption, and diffusion, which tends to homogenize variations. For a depth interval  
725 where there is no significant continuing acetate production and over which diffusive transport is limited,  
726 i.e.,  $(L/Dt)^{0.5} < 1$  (where D is the effective diffusion coefficient, L is the length scale and t is time),  $\delta^{13}\text{C}$ -  
727 acetate is expected to vary linearly with  $\ln([Ac]/[Ac]_0)$  (where  $[Ac]_0$  is the initial acetate concentration),  
728 with a slope of the isotope fractionation,  $\epsilon$ . In a diffusive steady state system with either zero or first  
729 order uptake kinetics, concentrations are zero at the boundary and the slope should be  $\epsilon/2$ . In systems  
730 where there is diffusion but steady-state has not been reached, the slope is expected to be between  
731 these values.

732 As expected, if biological uptake caused the acetate depletion in the deep cell populated zone,  $\delta^{13}\text{C}$ -  
733 acetate varies linearly as a function of  $\ln([Ac]/[Ac]_0)$  (fig. S10). With a best-fit slope of  $-7.7\%$ , the  
734 corresponding  $\epsilon$  value is ranging from  $-7.7\%$  to  $-15.4\%$ . This is consistent with the range of  
735 experimentally determined  $\epsilon$  values associated with biological acetate utilization (26).

736 We estimated the magnitude of the uptake with a simple model. First, we estimated the magnitude of  
737 thermogenic production based on acetate concentrations between ~650 and ~940 mbsf. In this zone of  
738 constant  $\delta^{13}\text{C}$ -acetate, which indicates the lack of uptake, concentrations rise rapidly and then  
739 approximately plateau. Since diffusion will only be effective over distances less than approximately 50 m  
740 in this region over the timescales since burial-driven heating began producing acetate 0.4 Ma, this  
741 plateau implies that the presumably dominantly thermogenic production is rapid as the sediment is  
742 heated to the acetate producing temperature window. Production then slows dramatically with further  
743 burial and heating, as otherwise concentrations would significantly rise with depth. The total production  
744 of acetate in each unit of sediment has thus been approximately  $9.2 \pm 2.4$  mM, while in our deepest  
745 sample concentration has been reduced to 3.3 mM, which gives an average depletion rate since the time  
746 of acetate production 0.4 Ma of approximately  $5 \times 10^{-12}$  to  $7 \times 10^{-12}$  mol  $\text{cm}^{-3} \text{y}^{-1}$ . Normalized to the  
747 abundance of cells in the cell populated zone ( $10$ - $100$  cells  $\text{cm}^{-3}$ ), the average uptake rates over the time  
748 since acetate was produced are between  $5 \times 10^{-14}$  to  $7 \times 10^{-13}$  mol cell $^{-1} \text{y}^{-1}$ .

749

750 7. Radiotracer experiments (Fig. 2E)

751 Metabolic activity of methanogenesis from CO<sub>2</sub> was determined in radiotracer experiments to achieve  
752 the highest possible sensitivity. Sediment was amended with seawater medium, traces of hydrogen, and  
753 <sup>14</sup>C-bicarbonate, and incubated in gas-tight headspace vials at representative in-situ temperatures. At  
754 the end of the experiments, radioactivity of the methane and bicarbonate pool was determined to  
755 quantify the rate of methane production. The resulting methanogenesis rates (MGR<sub>DIC</sub>) should be  
756 regarded as potential activity.

757 For radiotracer experiments, one peeled WRC sample (approx. length 10 cm) per investigated core was  
758 transferred to an anaerobic chamber. In the glove box, additional sediment (ca. 2-3 mm) was removed  
759 from the WRC surface with a sterile ceramic knife and discarded. The clean innermost part of the core  
760 was chopped off with the knife to create a mixture of very small sediment chips and powder.  
761 Approximately 5 mL of this sediment was placed into a 20-mL crimp vial to which 5 mL of artificial  
762 seawater medium (sulfate-free, 1 mM NaHCO<sub>3</sub>) were added (see recipe below). Three replicate vials  
763 were prepared from each WRC. Vials were crimp-sealed with chlorobutyl stoppers (Bellco) and  
764 aluminum crimps. After sealing, the vial headspace was flushed with N<sub>2</sub> gas to remove any hydrogen and  
765 other gases present in the atmosphere of the anaerobic chamber. Subsequently, 40 µL N<sub>2</sub>/H<sub>2</sub> gas  
766 (95%/5%) was injected into each vial to provide approx. 130 nM of dissolved hydrogen in the liquid  
767 phase. All vials and stoppers were autoclaved, and solutions were either autoclaved or filtered through  
768 sterile syringe filters (0.22 µm pore size) prior to use.

769 Radiotracer experiments were conducted in the radioisotope van onboard *Chikyu*. For the determination  
770 of MGR<sub>DIC</sub>, about 10 µL of radiolabeled (<sup>14</sup>C) NaHCO<sub>3</sub><sup>-</sup> (containing up to 3.7 MBq radioactivity) were  
771 injected through the rubber stoppers, and vials were shaken thoroughly. Samples were incubated at  
772 temperatures within the in-situ range: 40°C for ≤ 360 mbsf, 60°C for 405-585 mbsf, 80°C for 604-775  
773 mbsf and 95°C for ≥ 816 mbsf. After 5-10 days of incubation, microbial activity was stopped by injecting  
774 500 µL 50% NaOH (w/v) into each vial, and vials were shaken and shipped to Aarhus University,  
775 Denmark, for analysis.

776 The radiotracer experiments were accompanied by a suite of controls. On-board *Chikyu*, sediment  
777 controls (5 mL sediment mixed with 5 mL artificial, sulfate-free seawater medium) were incubated  
778 without radiotracer addition. Radiotracer was then added after microbial activity was stopped to check  
779 for reactions past incubation. In addition, medium controls (5 mL sterile medium, no sediment) and drill  
780 fluids (5 mL drill fluid, both seawater and high viscosity samples from the mud tank) were incubated with  
781 radiotracer in the same manner as sediment samples to check for non-biological reactions in the medium  
782 and biological reactions in the drill fluid, respectively. Moreover, an additional set of killed sediment  
783 controls was prepared post-cruise by irradiating sediment with 18 kGy. After irradiation, samples were  
784 incubated and processed like regular sediment samples.

785 Artificial seawater medium for sediment slurry incubations was prepared as follows. The subsequent  
786 salts were added to a 2-L glass bottle: 400 mg KH<sub>2</sub>PO<sub>4</sub>, 500 mg NH<sub>4</sub>Cl, 1 g MgCl<sub>2</sub> x 6H<sub>2</sub>O, 1 g KCl, 300 mg  
787 CaCl<sub>2</sub> x 2H<sub>2</sub>O, 50 g NaCl. The bottle was filled up to 2 L with ultrapure H<sub>2</sub>O. Some drops of Resazurin  
788 solution (100 mg Resazurin in 100 mL H<sub>2</sub>O) were added. The bottle was covered (but not completely  
789 closed) with a screw cap and autoclaved. After autoclaving, the medium was purged with N<sub>2</sub> gas while  
790 still hot (>60°C). During purging, 10 mL of sterile filtered NaHCO<sub>3</sub> solution (84 g NaHCO<sub>3</sub> in 100 ml H<sub>2</sub>O)  
791 were added to the medium. The pH was adjusted to 7.5 with sterile filtered 6.5% HCl (v/v) or NaOH  
792 solution (w/w). The bottle was then closed with a sterile butyl stopper and a screw cap and ~3 mL of



793 sterile filtered Na<sub>2</sub>S solution (1.2 g Na<sub>2</sub>S in 100 mL H<sub>2</sub>O) was added through the stopper with a syringe to  
794 reduce the medium. Reduction was confirmed by discoloration of Resazurin.

795 In each crimped vial, the amount of radioactive methane (<sup>14</sup>CH<sub>4</sub>) was determined using a method  
796 involving purging of the headspace, followed by combustion of <sup>14</sup>CH<sub>4</sub> from the headspace to <sup>14</sup>CO<sub>2</sub>, and  
797 scintillation counting (29). More specifically, the headspace was flushed with CO<sub>2</sub>-free air at 25 mL min<sup>-1</sup>  
798 for 20 min. In the evolving gas stream, <sup>14</sup>CH<sub>4</sub> was oxidized to <sup>14</sup>CO<sub>2</sub> in a quartz glass tube containing CuO  
799 pellets, heated to 900°C. <sup>14</sup>CO<sub>2</sub> from the oven exhaust gas was trapped in 5 mL Carbosorb (Perkin Elmer).  
800 The Carbosorb was mixed with 5 mL scintillation cocktail (Permafluor, PerkinElmer) and radioactivity of  
801 <sup>14</sup>CO<sub>2</sub> was quantified on a TriCarb 2900TR liquid scintillation analyzer (PerkinElmer). The entire gas line  
802 was made of glass, which does not absorb CO<sub>2</sub>, and the gas stream was subjected to a wash-step in 1 M  
803 NaOH before combustion to prevent trace amounts of labeled DIC from penetrating into the oven. The  
804 efficiency of CH<sub>4</sub> combustion was tested by adding known amounts of non-radioactive CH<sub>4</sub> to a reaction  
805 vessel and following its conversion to CO<sub>2</sub> in the exhaust gas. For this, 500 µL of the exhaust gas was  
806 regularly injected into a gas chromatograph equipped with a 0.9-m packed silica gel column of 3.1 mm  
807 inner diameter and a flame ionization detector (SRI 310C, SRI Instruments). Conversion efficiencies were  
808 always >99%.

809 After extraction of <sup>14</sup>CH<sub>4</sub>, a subsample of the sediment slurry (100 to 250 µL) was transferred into a new  
810 glass vial, crimp capped with butyl rubber stoppers, and acidified with 2 mL of HCl (6 M) to determine  
811 the remaining [<sup>14</sup>C]-DIC in the sediment. All produced <sup>14</sup>CO<sub>2</sub> was flushed out of the vial headspace with N<sub>2</sub>  
812 at 25 mL min<sup>-1</sup> for 35 min and trapped in 5 mL Carbosorb. The radioactivity of <sup>14</sup>CO<sub>2</sub> was counted in 5 mL  
813 scintillation cocktail (Permafluor, PerkinElmer) on a TriCarb 2900TR liquid scintillation analyzer  
814 (PerkinElmer).

815 MGR<sub>DIC</sub> were calculated similar to (29):

$$816 \quad \text{MGR}_{\text{DIC}} = (A_{\text{CH}_4} / [A_{\text{CH}_4} + A_{\text{DIC}}]) \times [\text{DIC}] \times 1.08 \times \rho / (t \times m) \quad (11)$$

817 if

$$818 \quad A_{\text{CH}_4} > [b_c + (3 \times \sigma_{bc})] \quad (12)$$

819 where  $A_{\text{CH}_4}$  is the radioactivity (counts per minute = CPM) of CH<sub>4</sub> at the end of the incubation,  $A_{\text{DIC}}$  is the  
820 radioactivity (CPM) of DIC at the end of the incubation,  $[\text{DIC}]$  is the amount (pmol) of DIC in the sample  
821 medium based on the DIC concentration in the medium (0.677 mM) and in the natural sediment  
822 porewater,  $1.08$  is the correction factor for the expected isotopic fractionation (81),  $\rho$  is the bulk  
823 sediment density (g cm<sup>-3</sup>),  $t$  is the incubation time (d),  $m$  is the sediment mass (g),  $b_c$  is the scintillation  
824 counter blank signal and  $\sigma_{bc}$  is the standard deviation of the blank signal. <sup>14</sup>CH<sub>4</sub> radioactivity determined  
825 in controls (sediment controls, medium controls, drill fluid, killed sediment controls) was within or close  
826 to levels of scintillation counter blanks. A conservative minimum quantification limit for biological tracer  
827 turnover of 0.094 pmol CH<sub>4</sub> cm<sup>-3</sup> d<sup>-1</sup> was calculated from the average activity measured in the killed  
828 control incubations plus 3 times the standard deviation. The down-hole profile of potential  
829 methanogenesis rates in Fig. 2E shows averages and standard deviations of three replicates (table S2).

830

## References

35. A. Taira, I. Hill, J.V. Firth *et al.*, *Proceedings of the Ocean Drilling Program, Initial Reports, 131*. (Ocean Drilling Program, College Station, Texas, 1991). <http://dx.doi.org/10.2973/odp.proc.ir.131.1991>
36. R. Harris *et al.*, A synthesis of heat flow determinations and thermal modeling along the Nankai Trough, Japan. *J. Geophys. Res.-Solid Earth* **118**, 2687-2702 (2013).
37. F. Inagaki, M. Kinoshita, A. Ijiri, K. Akiyama, V.B. Heuer, K. Homola, C. Li, T. Morisawa, Y. Morono, D. Pan, T. Sun, M.-Y. Tsang, T. Toki, and IODP Expedition 370 Scientists. JAMSTEC KR18-04 cruise report: Recovery of 1.5 years-temperature observatory data and shallow piston-core sediments from IODP Site C0023. KAIREI KR18-04 Cruise Data, JAMSTEC, pp. 1-21, (2018). doi:10.17596/0001270. <http://www.godac.jamstec.go.jp/darwin/cruise/kairei/kr18-04/e>
38. K. Hagino, the Expedition 370 Scientists, Data report: calcareous nannofossils from the middle Miocene to Pleistocene, IODP expedition 370 Site C0023. In: V.B. Heuer, F. Inagaki, Y. Morono, Y. Kubo, L. Maeda (Eds.), The Expedition 370 Scientists, Temperature Limit of the Deep Biosphere off Muroto. *Proceedings of the International Ocean Discovery Program, 370*, College Station, TX (International Ocean Discovery Program) (2018)
39. P. Costa Pisani, M. Reshef, G. Moore, Targeted 3-D prestack depth imaging at Legs 190-196 ODP drill sites (Nankai Trough, Japan). *Geophys. Res. Lett.* **32** (2005).
40. G. A. Spinelli *et al.*, Diagenesis, sediment strength, and pore collapse in sediment approaching the Nankai Trough subduction zone. *Geol. Soc. Am. Bull.* **119**, 377-390 (2007).
41. K. Gamage, E. Sreaton, Characterization of excess pore pressures at the toe of the Nankai accretionary complex, Ocean Drilling Program sites 1173, 1174, and 808: Results of one-dimensional modeling. *J. Geophys. Res.-Solid Earth* **111**, 13 (2006).
42. T. Tsuji, H. Tokuyama, P. Costa Pisani, G. Moore, Effective stress and pore pressure in the Nankai accretionary prism off the Muroto Peninsula, southwestern Japan. *Journal of Geophysical Research: Solid Earth* **113**, (2008).
43. H. Tobin, P. Vannucchi, M. Meschede, Structure, inferred mechanical properties, and implications for fluid transport in the décollement zone, Costa Rica convergent margin. *Geology* **29**, 907-910 (2001).
44. H. J. Tobin, D. M. Saffer, Elevated fluid pressure and extreme mechanical weakness of a plate boundary thrust, Nankai Trough subduction zone. *Geology* **37**, 679-682 (2009).
45. D. R. Faulkner *et al.*, A review of recent developments concerning the structure, mechanics and fluid flow properties of fault zones. *J. Struct. Geol.* **32**, 1557-1575 (2010).
46. K. M. Brown, D. M. Saffer, B. A. Bekins, Smectite diagenesis, pore-water freshening, and fluid flow at the toe of the Nankai wedge. *Earth Planet. Sci. Lett.* **194**, 97-109 (2001).
47. P. Henry, L. Jouniaux, E. J. Sreaton, S. Hunze, D. M. Saffer, Anisotropy of electrical conductivity record of initial strain at the toe of the Nankai accretionary wedge. *Journal of Geophysical Research: Solid Earth* **108**, (2003).
48. M. Kastner *et al.*, 32. Geochemical and isotopic evidence for fluid flow in the western Nankai subduction zone Japan. *Proceedings of the Ocean Drilling Program. Sci Results* **131**, 397-413 (1993).
49. A. J. Spivack, M. Kastner, B. Ransom, Elemental and Isotopic Chloride Geochemistry and Fluid Flow in the Nankai Trough. *Geophys. Res. Lett.* **29**, 6-1-6-4 (2002).
50. S. Tonai *et al.*, A New Method for Quality Control of Geological Cores by X-Ray Computed Tomography: Application in IODP Expedition 370. *Frontiers in Earth Science* **7**, (2019).

51. E.C. Bullard, Heat flow in South Africa. *Proc. R. Soc. London, Ser. A*, **173**, 474–502 (1939). doi:10.1098/rspa.1939.0159
52. E. Buckingham, On Physically Similar Systems; Illustrations of the Use of Dimensional Equations. *Physical Review* **4**, 345-376 (1914).
53. M. Heesemann *et al.*, Data report: testing and deployment of the new APCT-3 tool to determine in situ temperatures while piston coring. In: Riedel M, Collett TS, Malone MJ, *et al.* (Eds.) *Proceedings of the Integrated Ocean Drilling Program*, 311. (Washington, DC, Integrated Ocean Drilling Program Management International, 2006). doi:10.2204/iodp.proc.311.108.2006
54. M. Kinoshita, H. Fukase, S. Goto, T. Toki, In situ thermal excursions detected in the Nankai Trough forearc slope sediment at IODP NanTroSEIZE Site C0008. *Earth, Planets and Space* **67**, 16 (2015).
55. Y. Morono, F. Inagaki, Chapter Three-Analysis of Low-Biomass Microbial Communities in the Deep Biosphere. *Advances in Applied Microbiology* **95**, 149-178 (2016).
56. Y. Morono, T. Terada, J. Kallmeyer, F. Inagaki, An improved cell separation technique for marine subsurface sediments: applications for high-throughput analysis using flow cytometry and cell sorting. *Environ. Microbiol.* **15**, 2841-2849 (2013).
57. Kallmeyer, J., Smith, D.C., D'Hondt, S.L. and Spivack, A.J. New cell extraction procedure applied to deep subsurface sediments. *Limnology and Oceanography: Methods* **6**, 236-245 (2008).
58. Y. Morono, T. Terada, N. Masui, F. Inagaki, Discriminative detection and enumeration of microbial life in marine subsurface sediments. *ISME Journal* **3**, 503-511 (2009).
59. B. Lomstein, A. Langerhuus, S. D'Hondt, B. Jørgensen, A. Spivack, Endospore abundance, microbial growth and necromass turnover in deep sub-seafloor sediment. *Nature* **484**, 101-104 (2012).
60. Y. Morono *et al.*, Assessment of Capacity to Capture DNA Aerosols by Clean Filters for Molecular Biology Experiments. *Microbes and Environments* **33**, 222-226 (2018).
61. Y. Morono *et al.*, Intact preservation of environmental samples by freezing under an alternating magnetic field. *Environmental Microbiology Reports* **7**, 243-251 (2015).
62. J. Fichtel, J. Köster, J. Rullkötter, H. Sass, High Variations in Endospore Numbers within Tidal Flat Sediments Revealed by Quantification of Dipicolinic Acid. *Geomicrobiol. J.* **25**, 371-380 (2008).
63. J. Fichtel, J. Koster, B. Scholz-Bottcher, H. Sass, J. Rullkotter, A highly sensitive HPLC method for determination of nanomolar concentrations of dipicolinic acid, a characteristic constituent of bacterial endospores. *J. Microbiol. Methods* **70**, 319-327 (2007b).
64. J. Fichtel, J. Koster, J. Rullkotter, H. Sass, Spore dipicolinic acid contents used for estimating the number of endospores in sediments. *FEMS Microbiol. Ecol.* **61**, 522-532 (2007).
65. J. F. Biddle, S. Fitz-Gibbon, S. C. Schuster, J. E. Brenchley, C. H. House, Metagenomic signatures of the Peru Margin subseafloor biosphere show a genetically distinct environment. *Proc. Natl. Acad. Sci. U. S. A.* **105**, 10583-10588 (2008).
66. J. C. Fry, R. J. Parkes, B. A. Cragg, A. J. Weightman, G. Webster, Prokaryotic biodiversity and activity in the deep subseafloor biosphere. *FEMS Microbiol. Ecol.* **66**, 181-196 (2008).
67. D. Zhu, S. H. Tanabe, C. Yang, W. Zhang, J. Sun, Bacterial community composition of South China Sea sediments through pyrosequencing-based analysis of 16S rRNA genes. *PloS one* **8**, e78501 (2013).
68. F. Inagaki *et al.*, Biogeographical distribution and diversity of microbes in methane hydrate-bearing deep marine sediments, on the Pacific Ocean Margin. *Proc. Natl. Acad. Sci. U. S. A.* **103**, 2815-2820 (2006).

69. M. Kawai, I. Uchiyama, H. Takami, F. Inagaki, Low frequency of endospore-specific genes in subseafloor sedimentary metagenomes. *Environmental Microbiology Reports* **7**, 341-350 (2015).
70. W. L. Nicholson, Using thermal inactivation kinetics to calculate the probability of extreme spore longevity: Implications for paleomicrobiology and lithopanspermia. *Orig. Life Evol. Biosph.* **33**, 621–631 (2003).
71. P. De Vos, G. Garrity, D. Jones, N. R. Krieg, W. Ludwig, F. A. Rainey, K. H. Schleifer, W. B. Whitman, Eds., *Bergey's Manual of Systematic Bacteriology: Volume 3: The Firmicutes* (Springer, New York, 2009).
72. V. Heuer *et al.*, Online  $\delta^{13}\text{C}$  analysis of volatile fatty acids in sediment/porewater systems by liquid chromatography-isotope ratio-mass spectrometry. *Limnology and Oceanography: Methods* **4**, 346-357 (2006).
73. M. P. Ricci, D. A. Merritt, K. H. Freeman, J. M. Hayes, Acquisition and processing of data for isotope-ratio-monitoring mass spectrometry. *Org. Geochem.* **21**, 561-571 (1994).
74. J. Santrock, S. A. Studley, J. M. Hayes, Isotopic Analyses Based on the Mass-Spectrum of Carbon-Dioxide. *Anal. Chem.* **57**, 1444-1448 (1985).
75. J. W. Johnson, E. H. Oelkers, H. C. Helgeson, SUPCRT92: A software package for calculating the standard molal thermodynamic properties of minerals, gases, aqueous species, and reactions from 1 to 5000 bar and 0 to 1000 C. *Computers & Geosciences* **18**, 899-947 (1992).
76. E. L. Shock, H. C. Helgeson, Calculation of the thermodynamic and transport properties of aqueous species at high pressures and temperatures: Correlation algorithms for ionic species and equation of state predictions to 5 kb and 1000°C. *Geochim. Cosmochim. Acta* **52**, 2009-2036 (1988).
77. E. L. Shock, H. C. Helgeson, Calculation of the thermodynamic and transport properties of aqueous species at high pressures and temperatures: Standard partial molal properties of organic species. *Geochim. Cosmochim. Acta* **54**, 915-945 (1990).
78. E. L. Shock, Organic acids in hydrothermal solutions; standard molal thermodynamic properties of carboxylic acids and estimates of dissociation constants at high temperatures and pressures. *Am. J. Sci.* **295**, 496-580 (1995).
79. H. C. Helgeson, Thermodynamics of hydrothermal systems at elevated temperatures and pressures. *Am. J. Sci.* **267**, 729-804 (1969).
80. V. B. Heuer, M. Krüger, M. Elvert, K.-U. Hinrichs, Experimental studies on the stable carbon isotope biogeochemistry of acetate in lake sediments. *Org. Geochem.* **41**, 22-30 (2010).
81. L. K. Hansen, R. Jakobsen, D. Postma D, Methanogenesis in a shallow sandy aquifer, Rømø, Denmark. *Geochim Cosmochim Acta* **65**, 2925–2935 (2001).

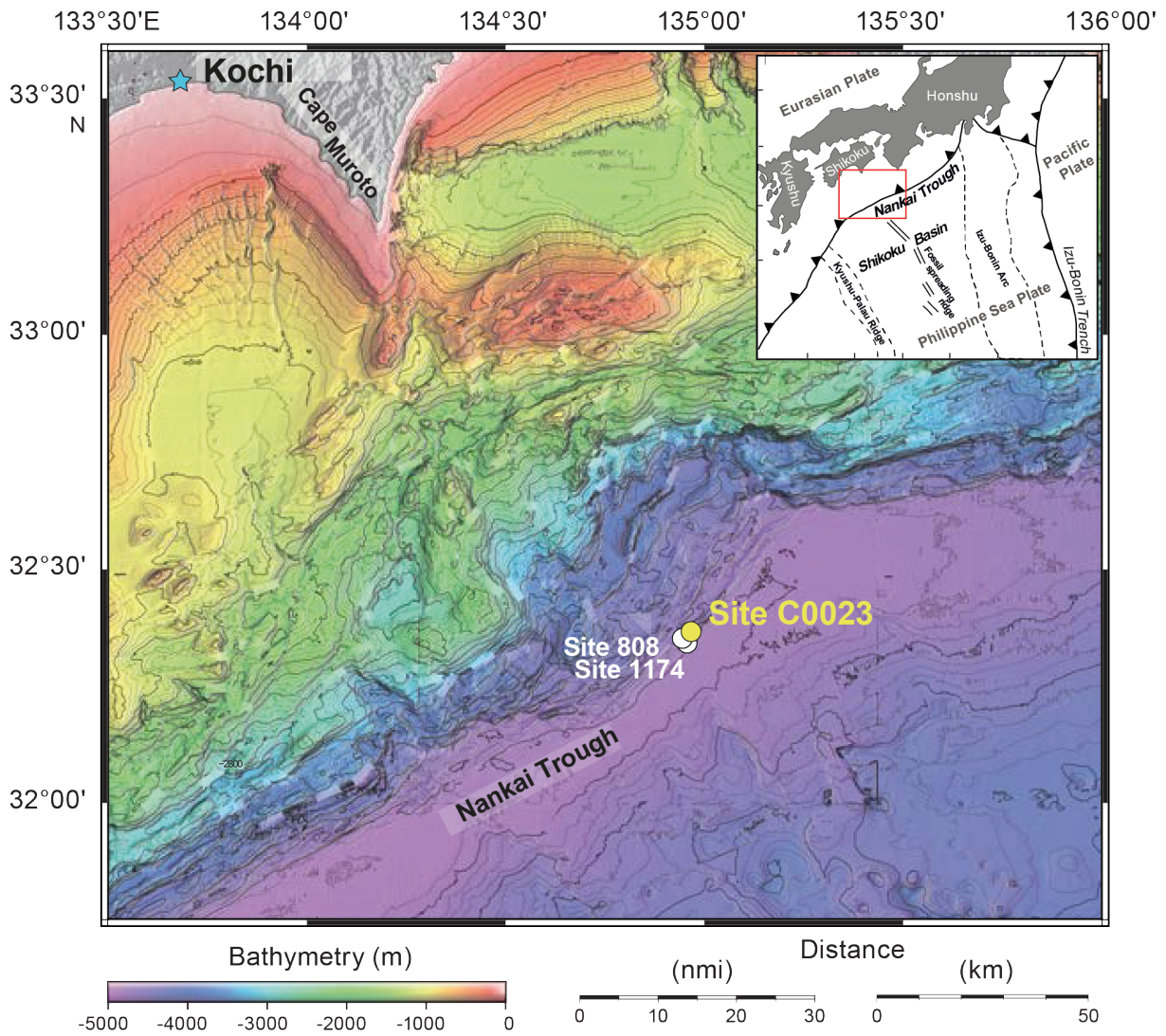


**Fig. S1. Bathymetric map showing IODP Site C0023 drilled by the *DV Chikyu* in 2016 (IODP Expedition 370) off Cape Muroto, Japan, together with previously existing ODP Sites 808 and 1174 drilled by the *DV JOIDES Resolution* in 1990 and 2000, respectively. Inset map shows the location (red square) within the context of the general tectonic configuration of the Japanese Island system. (Modified from ref. 14).**

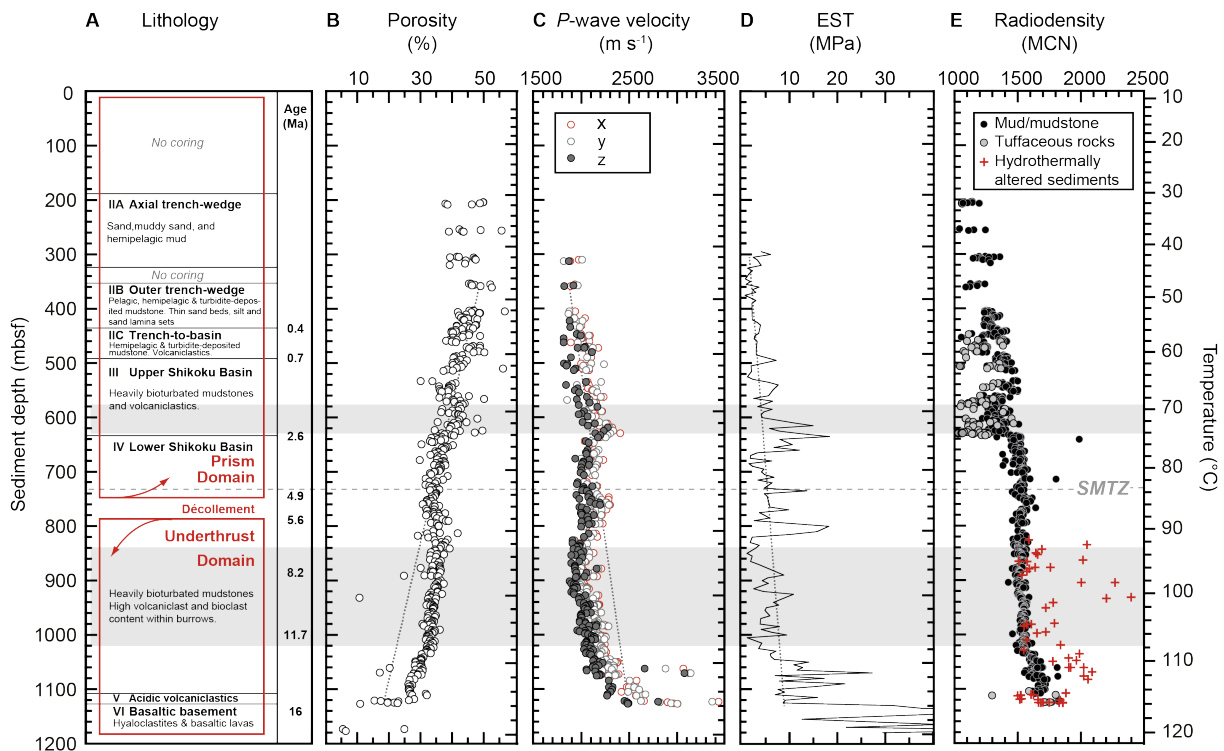


**Fig. S2. Depth profiles of sedimentological properties at IODP Site C0023.** (A) Lithostratigraphy, tectonic domains, and age information. Major lithological facies (black) are given together with core observations used to constrain formation boundaries (modified from ref. 14). Three tectonic domains (red) are separated based on deformation structures, i.e. an upper domain that comprises the prism, cut by low angle thrusts, the décollement zone at 758-796 mbsf, consisting of relatively thin, characteristically brecciated fault zones that are alternating with several meter thick intact zones, and an underthrust domain with extensional faulting and no thrust fault zones (14). The age model results from biostratigraphic studies based on calcareous nannofossil assemblages (38). (B) Porosities, inferred from moisture and density measurements of discrete sediment and rock samples, generally decrease with increasing depth. However, a distinct reversal of this trend (dotted line) occurs across and below the décollement (modified from ref. 14). (C) *P*-wave velocities, i.e. the speed at which ultrasonic sound waves pass through intact sediment cores in three-dimensional space (*x*, *y*, *z*), inversely reflect the porosity profile in general, except for a positive excursion of *P*-wave velocities from the down-hole trend (dotted line) at ~630 mbsf, pointing to a stiffening of the fine to coarse tuff and tuffaceous muds in this interval (modified from ref 15). (D) Equivalent strength (EST) is a measure for the in-situ strength of the geological formation, which is deduced from drilling parameters. Positive EST excursions from the down-hole trend (dotted line) show distinctly elevated mechanical strength in the tuff-rich sediments around ~630 mbsf, while negative EST excursions reveal a mechanically weak zone below the décollement (modified from ref. 33). (E) The radiodensity profile was derived from continuous logging of sediment cores by X-ray computed tomography (XCT), with average values of quality controlled mean CT number (MCN) in lithological intervals logged by visual core description (modified from ref. 50). In general, radiodensity increases with depth due to the compaction of mud and mudstones (black symbols). Negative and positive excursions reflect and record the presence of porous tuff layers (gray symbols) and dense hydrothermal mineral assemblages (red symbols), respectively. Gray shading indicates zones where concentrations of both vegetative cells and endospores were below the detection limits of the employed methods in all investigated samples (cf. Fig. 1). The horizontal dashed gray line indicates the location of the sulfate-methane transition zone (SMTZ) at ~730 mbsf (cf. Fig. 2).

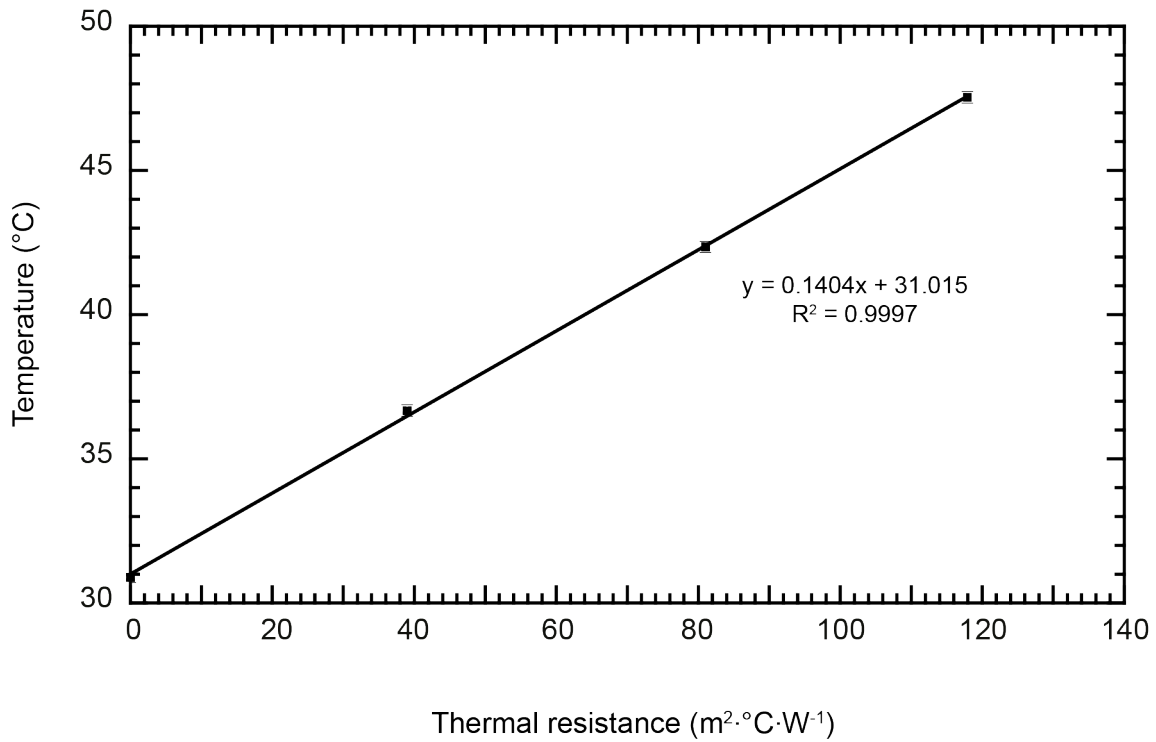


**Fig. S3. Heat flow estimate for IODP Site C0023.** Measured in-situ temperature vs. thermal resistance,  $\sum_{i=0}^N \left( \frac{\Delta z_i}{k(z)_i} \right)$ . The slope of the line is equal to  $-q$ , the negative of the heat flow,  $-0.1404 \text{ W m}^{-2}$  (51). The 90% confidence limit of the heat flow is  $0.005 \text{ W m}^{-2}$ . The error bars are the reported uncertainties of the measured temperature, 0.2%.

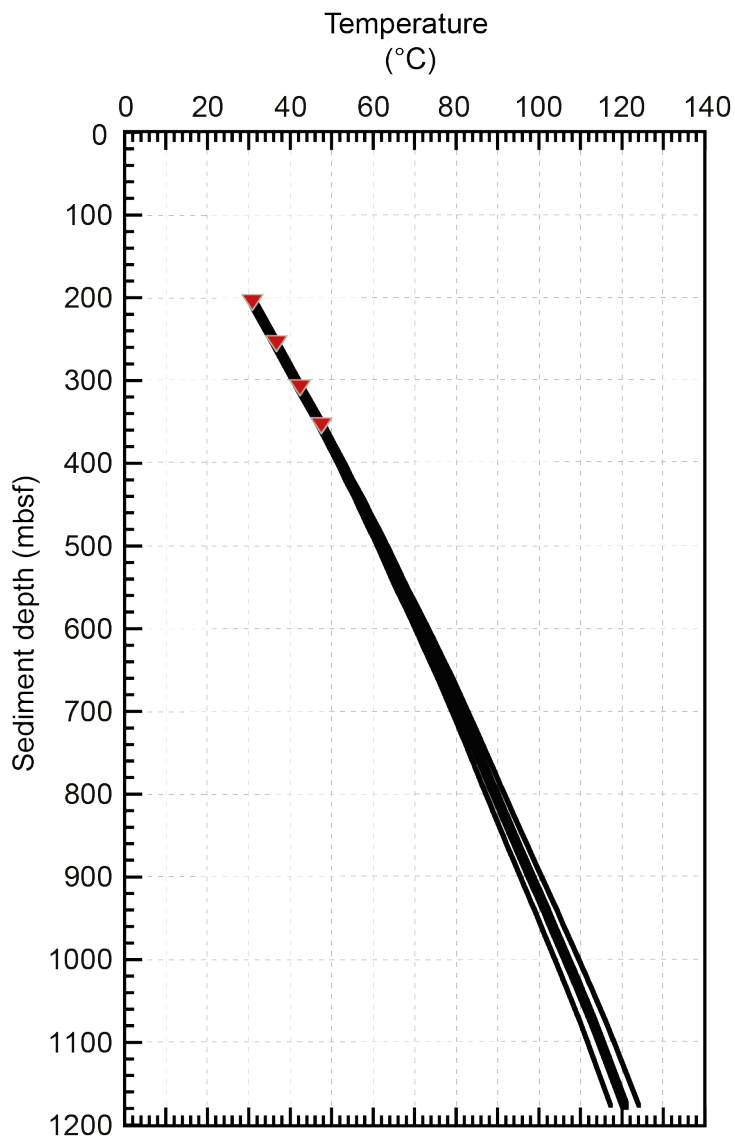


**Fig. S4. Temperature profile at Site C0023.** In-situ temperatures were determined based upon measured heat flow, thermal conductivities and application of the Bullard equation (equation 2) (51). The thick line is the best estimate and the thin lines represent the 90% confidence limits. The red triangles are in-situ temperatures measured by APCT-3 tool.



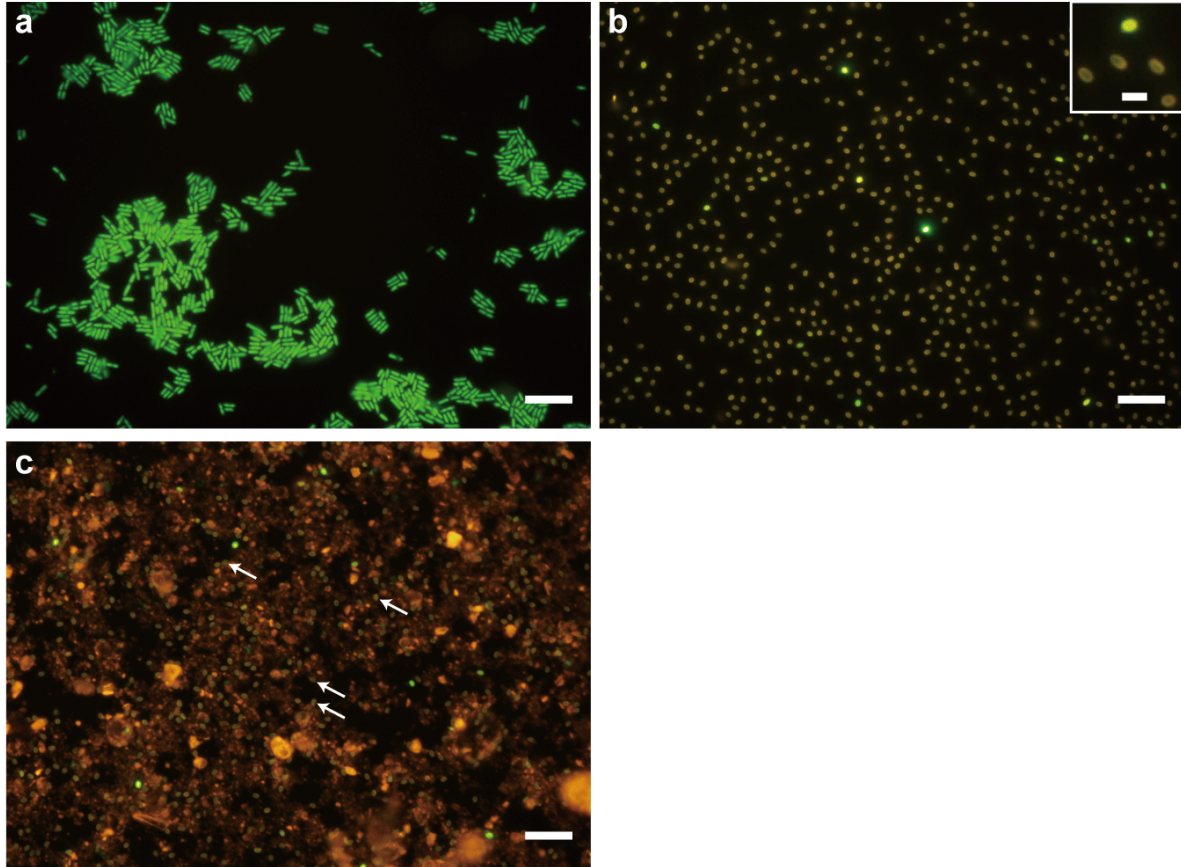


**Fig. S5. SYBR Green I staining of vegetative cells (a) and endospores (b) of *Bacillus subtilis* NBRC13719.** Close-up of the spores are shown in white box of (b). In (c), endospores were mixed in sterilized sediment prior to staining by SYBR Green I. Typical yellowish endospores, which are difficult to distinguish from sediment particles, are indicated by white arrows. Bars are 10  $\mu\text{m}$  (2  $\mu\text{m}$  in the white box of (b)).

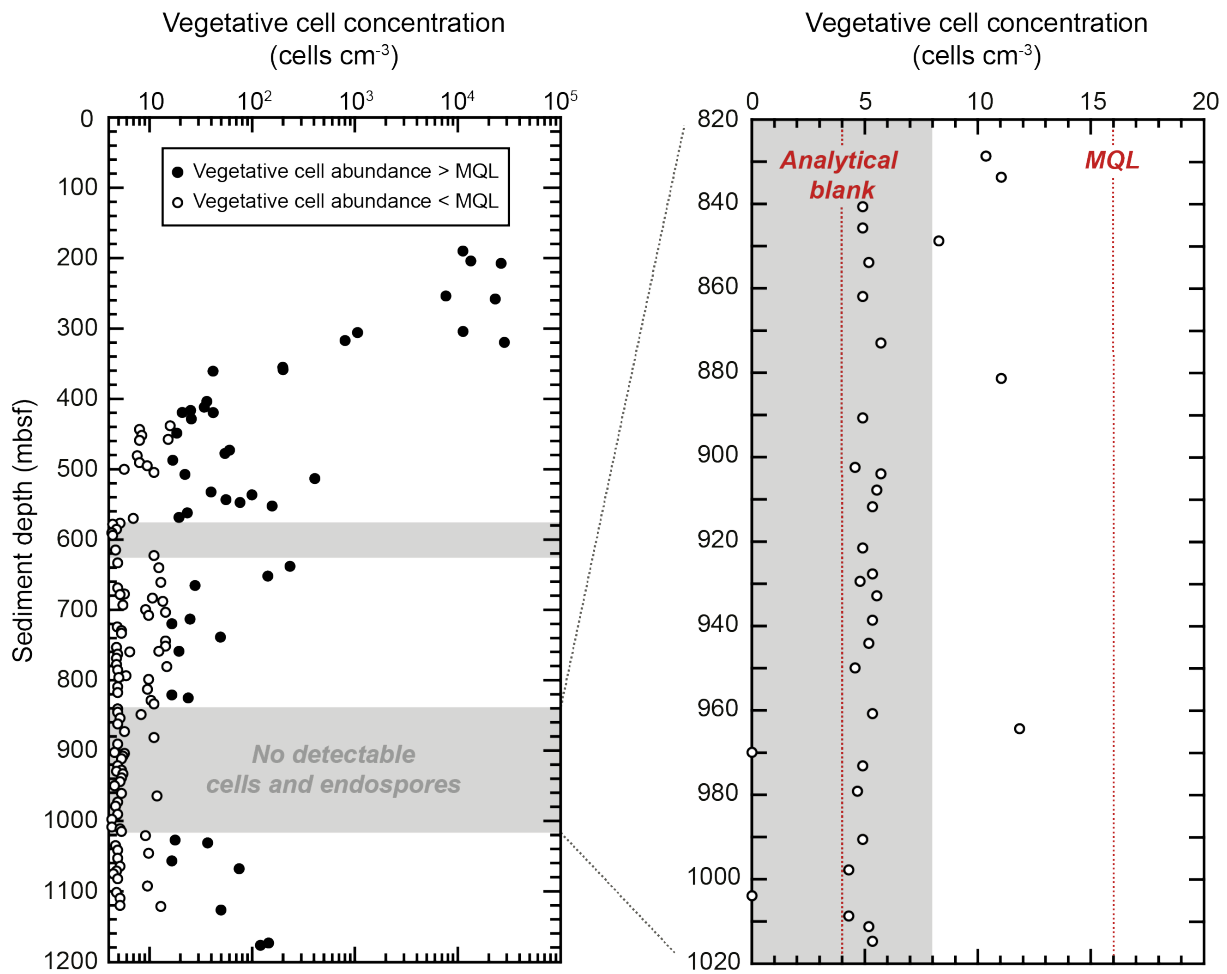


**Fig. S6. Absence of contaminant cells from drilling fluids in low biomass samples recovered from IODP Site C0023.** Concentrations of microbial cells fluorescently stained with SYBR Green I fall in the range of the analytical blank ( $4.2 \pm 4.0$  cells  $\text{cm}^{-3}$ ;  $N = 20$ ) or remain below the minimum quantification limit (MQL) of 16 cells  $\text{cm}^{-3}$  in 32 samples retrieved from 829 to 1020 mbsf. This finding shows that the introduction of contaminant cells was negligible during cutting, retrieval and processing of 21 successively taken rotary core barrel (RCB) cores on board *DV Chikyu*.

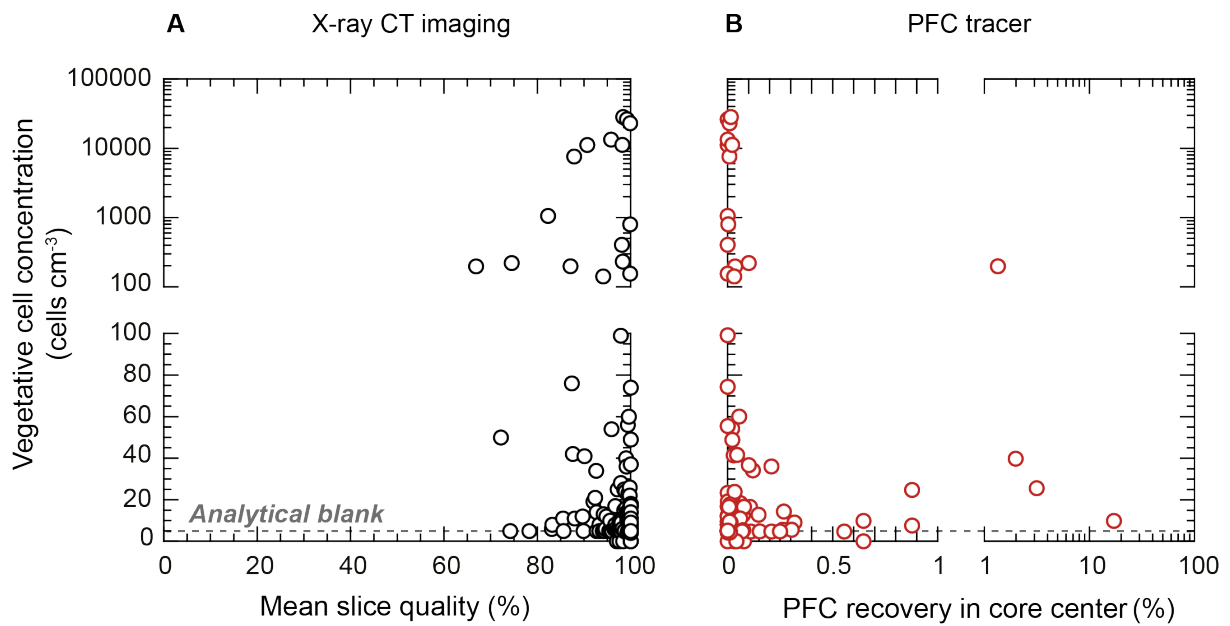


**Fig. S7 Impact of drilling on the concentration of vegetative cells in samples from Site C0023.** (A) Sample quality was assured using X-ray CT imaging for the selection of undisturbed core intervals, and controlled based on a quality assessment of individual 0.625 mm thick X-ray CT slice images. A mean slice quality of 100% in the sampled ~30 cm long core intervals represents the highest possible core quality. The lack of relation between mean slice quality and vegetative cell abundance shows that contamination due to the introduction of microbial cells along drilling induced fractures is negligible in high quality cores. (B) Established routines for contamination testing were applied to monitor the potential intrusion of drilling fluid into the cores with the perfluorocarbon (PFC) tracer perfluoromethylcyclohexane. PFC recovery normalizes the PFC concentration measured in the center part of an individual core to the average PFC concentration in the outer parts of the cores, which had been in direct contact with drilling fluid. A PFC recovery of 0% in the core center represents the lowest risk of drilling induced contamination. The lack of a relationship between PFC recovery and vegetative cell abundance indicates the absence of contamination due to diffusion or advection of drilling fluids. The dashed line represents the analytical blank of cell enumeration ( $4.2 \pm 4.0$  cells cm<sup>-3</sup>).

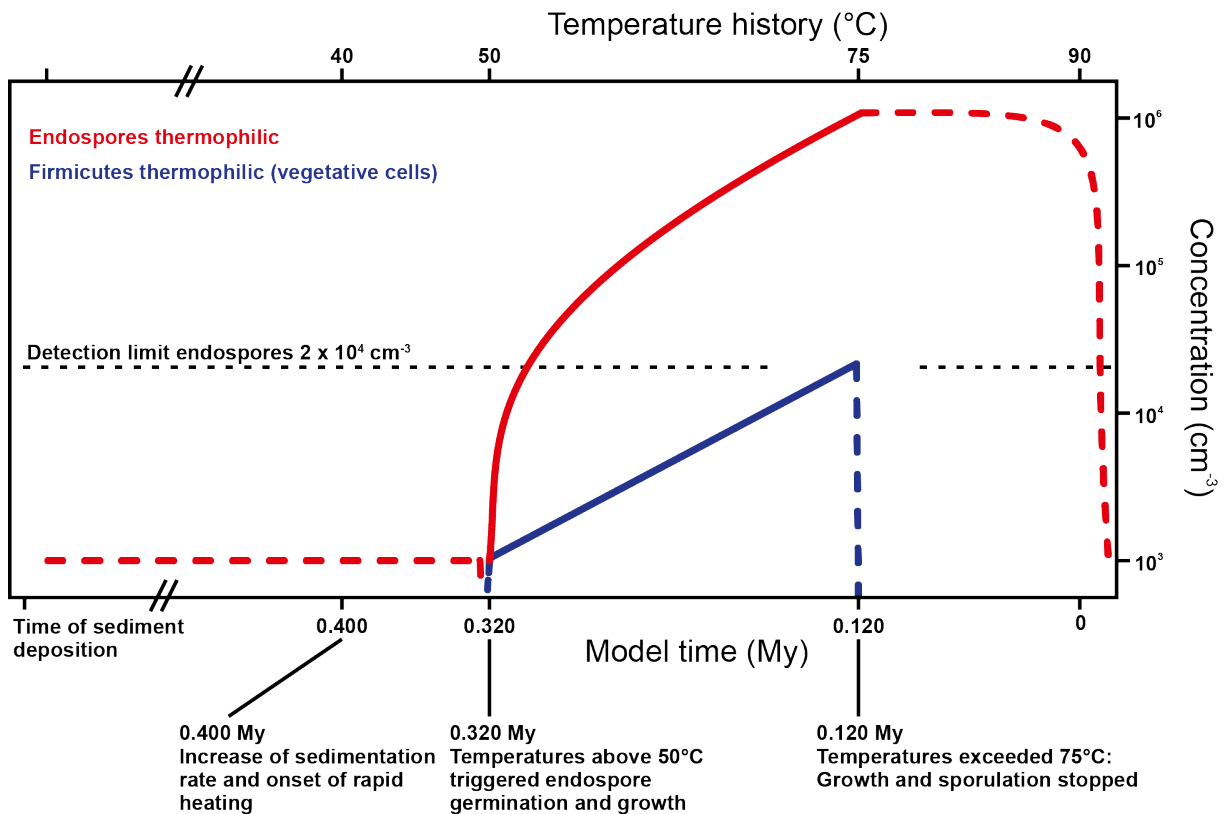


**Fig. S8. Validation of the observed accumulation of endospores ( $> 1 \times 10^6$  endospores  $\text{cm}^{-3}$ ; Fig. 1) within the sediment interval corresponding to the major endospore peak between 633-827 mbsf at Site C0023.** Depicted is the hypothetical temporal history of the concentrations of thermophilic endospores (solid red line) and vegetative Firmicutes (solid blue line) in the sediments corresponding to this peak through the time period characterized by intensified geothermal heating. Red and blue dashed lines are schematic and do not represent modeling outputs. High accumulation rates of trench sediments in the last 0.4 My caused rapid, linear heating of the sediments at a rate of  $\sim 125^\circ\text{C My}^{-1}$ . Our model assumes the presence of a background population of 1000 thermophilic endospores  $\text{cm}^{-3}$  (red dashed line; this value is lower than estimated background populations in young Arctic surface sediments (17) and was arbitrarily chosen to be lower than our detection limit) and initial germination of vegetative Firmicutes from these endospores at 0.32 Ma, when temperatures reached  $50^\circ\text{C}$ ; subsequent growth of the Firmicutes populations lasted for 0.2 My until sediment temperatures in this horizon had reached  $75^\circ\text{C}$ . Further details on the model parameters are presented in section 5.3 of the supplementary text. This model shows that the formation of the large endospore population ( $> 1 \times 10^6$  endospores  $\text{cm}^{-3}$ ) from germination of a small background population of thermophilic endospores and subsequent growth is plausible based on a set of reasonable assumptions such as a growth temperature range of  $50\text{-}75^\circ\text{C}$  for thermophiles and doubling time of 1290 years for vegetative cells, while still maintaining a relatively low vegetative cell population of below  $\sim 2 \times 10^4$  cells  $\text{cm}^{-3}$ .

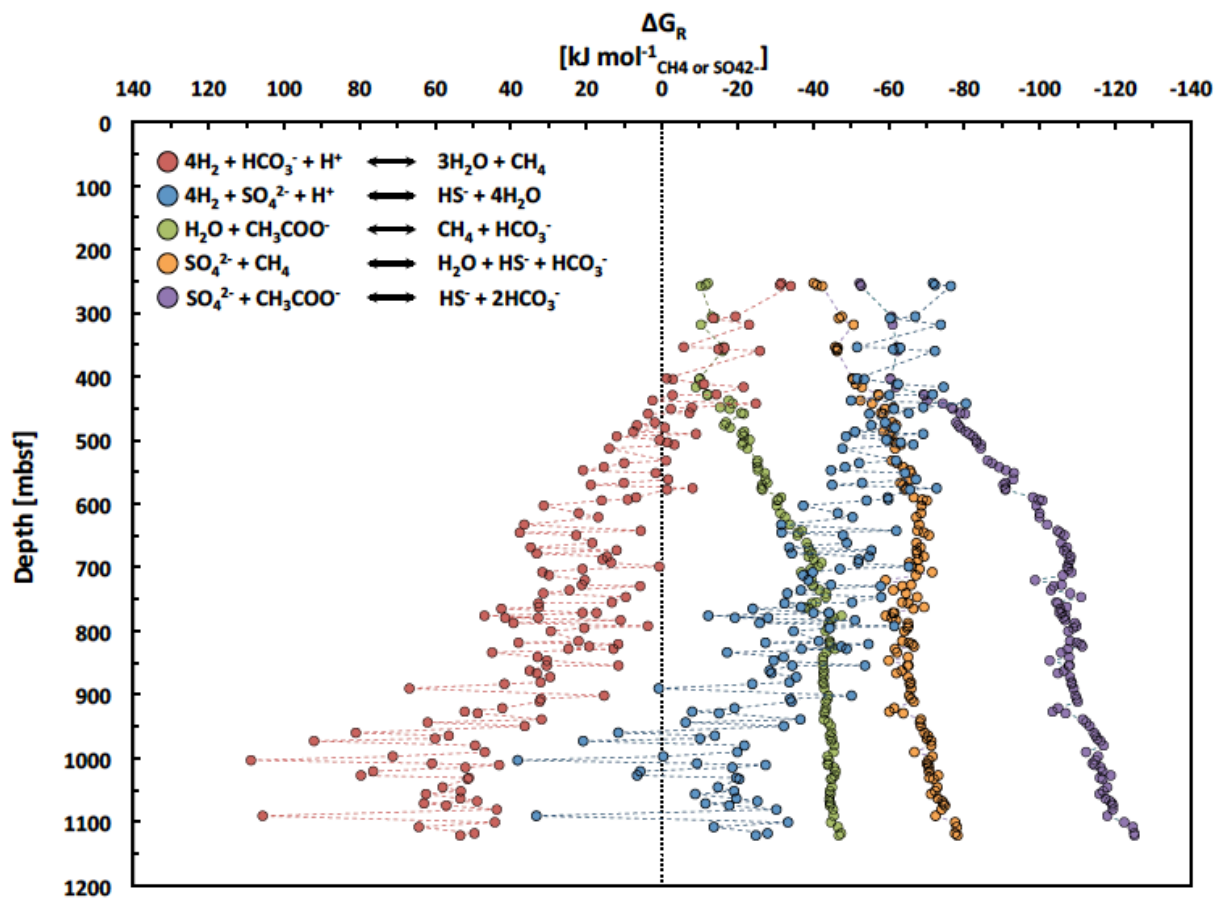
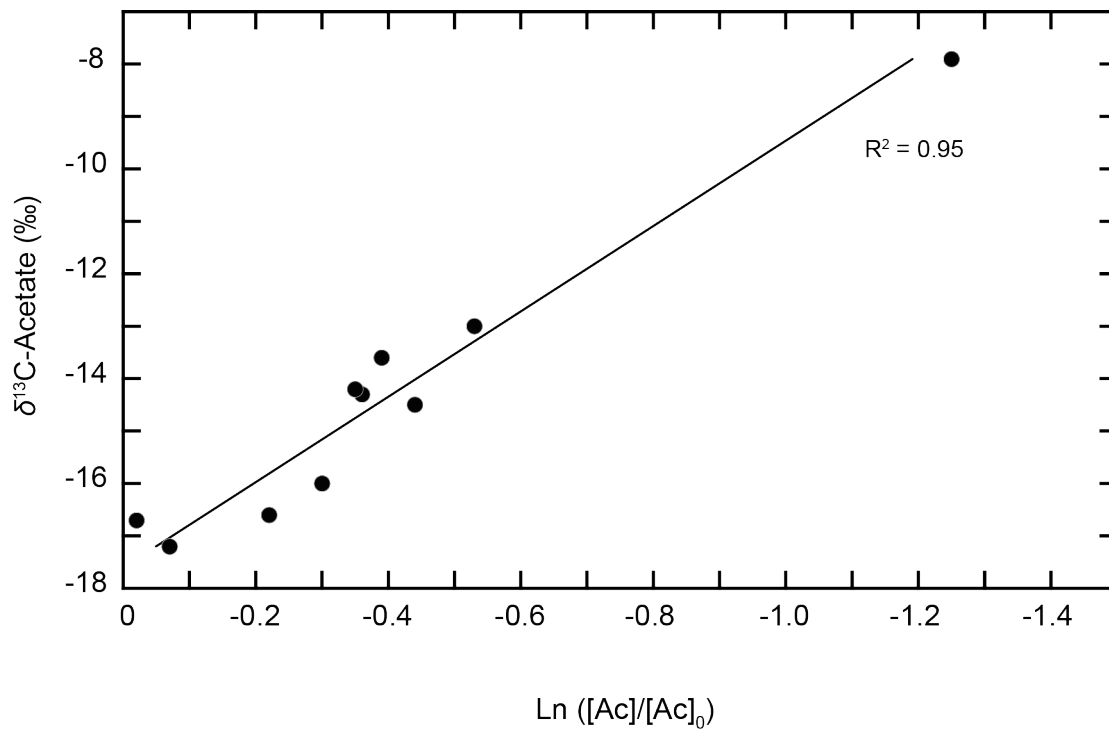


Fig. S9. Calculated Gibbs free energy yields of methanogenesis from hydrogen, sulfate reduction from hydrogen, methanogenesis from acetate, sulfate-dependent AOM, and sulfate reduction from acetate, in sediments at Site C0023.



**Fig. S10.  $\delta^{13}\text{C}$ -acetate diffusion-reaction model.** At the bottom of Hole C0023A, at 961-1101 mbsf, acetate concentrations  $[\text{Ac}]$  decrease and  $\delta^{13}\text{C}$ -acetate varies linearly as a function of  $\ln ([\text{Ac}]/[\text{Ac}]_0)$ , where  $[\text{Ac}]_0$  is the acetate concentration in the overlying stagnant acetate pool (i.e. a measured concentration of 11.7 mM at 929.71 mbsf, close to the upper range of average acetate concentrations of  $9.2 \pm 2.4$  mM at 593.45-945.21 mbsf,  $N = 47$ ). This relationship indicates biological uptake of acetate. The best-fit slope of  $-7.7\text{‰}$  is consistent with the range of experimentally determined isotopic fractionation factors associated with biological acetate utilization (26).

## Supporting tables

*Table S1: Endospore to vegetative cell ratios for different depth intervals. The upper interval boundary was approximated to the depth of the shallowest sample analyzed for endospores (250 mbsf) or the depth of the major decline of vegetative cell concentrations (350 mbsf). The lower boundary was set by the deepest endospore sample (1121 mbsf) or the sediment/basement boundary (1177 mbsf). Additionally, calculations using the endospore detection limit of  $2.2 \times 10^4$  endospores  $\text{cm}^{-3}$  are provided together with calculations, using the value of the analytical blank of vegetative cells as hypothetical detection limit (DL) for endospores (4 endospores  $\text{cm}^{-3}$ ).*

Interval	Ratio endospores/vegetative cell	
	DL = $2.2 \times 10^4$ endospores $\text{cm}^{-3}$	DL = 4 endospores $\text{cm}^{-3}$
250 mbsf – 1121 mbsf	120	110
250 mbsf – 1177 mbsf	120	110
350 mbsf – 1121 mbsf	8200	7700
350 mbsf – 1177 mbsf	6500	6100

Table S2: Potential methanogenesis rates from dissolved inorganic carbon determined in radiotracer experiments. AVG = average, StDEV = Standard deviation. Gray fields indicate average rates below the quantification limit ( $<0.094 \text{ pmol CH}_4 \text{ cm}^{-3} \text{ d}^{-1}$ ).

Depth [mbsf]	Replicate 1 Methane production [ $\text{pmol d}^{-1} \text{ cm}^{-3}$ ]	Replicate 2 Methane production [ $\text{pmol d}^{-1} \text{ cm}^{-3}$ ]	Replicate 3 Methane production [ $\text{pmol d}^{-1} \text{ cm}^{-3}$ ]	AVG Methane production [ $\text{pmol d}^{-1} \text{ cm}^{-3}$ ]	StDev Methane production [ $\text{pmol d}^{-1} \text{ cm}^{-3}$ ]
189	391.53	394.71	464.39	416.88	41.18
206	27.86	35.62	4.49	22.65	16.20
319	1.49	3.59	2.36	2.48	1.06
350	1.08	2.50	0.88	1.49	0.88
405	0.90	0.47	0.30	0.56	0.31
412	0.51	0.98	0.42	0.63	0.30
430	0.57	0.24	0.72	0.51	0.25
443	0.18	0.00	0.00	0.06	0.10
448	0.88	1.30	0.47	0.88	0.41
476	1.55	0.53	0.41	0.83	0.62
486	0.19	0.12	0.05	0.12	0.07
496	0.15	0.14	0.05	0.11	0.06
508	0.00	0.00	0.05	0.02	0.03
538	0.05	0.25	0.13	0.14	0.10
564	1.91	0.89	0.73	1.18	0.64
576	0.00	0.00	0.05	0.02	0.03
585	0.15	0.05	0.05	0.08	0.06
605	0.17	0.14	0.05	0.12	0.06
616	0.21	0.23	0.26	0.24	0.03
633	1.30	1.09	0.71	1.03	0.30
643	1.78	2.24	0.71	1.58	0.79
693	0.32	0.45	0.33	0.37	0.07
718	0.50	0.29	0.29	0.36	0.12
735	0.64	0.58	0.17	0.46	0.26
754	0.19	0.05	0.00	0.08	0.10
775	0.00	0.00	0.09	0.03	0.05
816	0.05	0.11	0.14	0.10	0.05
830	0.00	0.05	0.05	0.03	0.03
850	0.23	0.19	0.16	0.19	0.04
864	0.52	0.47	0.25	0.41	0.15
883	0.33	0.41	0.50	0.41	0.09
901	0.20	0.33	0.16	0.23	0.09
922	0.11	0.05	0.05	0.07	0.04
940	0.18	0.00	0.00	0.06	0.11
961	0.05	0.05	0.00	0.03	0.03
980	0.17	0.00	0.00	0.06	0.10
1003	0.00	0.05	0.00	0.02	0.03
1022	0.14	0.00	0.00	0.05	0.08
1042	0.00	0.00	0.05	0.02	0.03
1066	0.00	0.00	0.00	0.00	0.00
1094	1.96	2.17	1.86	2.00	0.16
1124	2.66	1.55	1.51	1.91	0.65
1177	1.12	1.26	2.11	1.50	0.53